The Astrophysical Journal, 927:66 (31pp), 2022 March 1 https://doi.org/10.3847/1538-4357/ac4270
© 2022. The Author(s). Published by the American Astronomical Society.
OPEN ACCESS

WALLABY Pre-pilot Survey: The Effects of Tidal Interaction on Radial Distribution of Color in Galaxies of the Eridanus Supergroup

Shun Wang[1,2], Jing Wang[1], Bi-Qing For[3], Bumhyun Lee[1], T. N. Reynolds[3,4], Xuchen Lin[5], L. Staveley-Smith[3], Li Shao[6], O. I. Wong[3,4,7], B. Catinella[3,4], P. Serra[8], L. Verdes-Montenegro[9], T. Westmeier[3], K. Lee-Waddell[3,7], B. S. Koribalski[10,11], C. Murugeshan[4,7], A. Elagali[12], D. Kleiner[8], J. Rhee[3,4], F. Bigiel[13], A. Bosma[14], B. W. Holwerda[15], S.-H. Oh[16], and K. Spekkens[17]

[1] Kavli Institute for Astronomy and Astrophysics, Peking University, Beijing 100871, People's Republic of China; jwang_astro@pku.edu.cn
[2] Department of Astronomy, School of Physics, Peking University, Beijing 100871, People's Republic of China
[3] ICRAR, The University of Western Australia, 35 Stirling Highway, Crawley WA 6009, Australia
[4] ARC Centre of Excellence for All Sky Astrophysics in 3 Dimensions (ASTRO 3D), Australia
[5] School of Physics, Peking University, Beijing 100871, People's Republic of China
[6] National Astronomical Observatories, Chinese Academy of Sciences, 20A Datun Road, Chaoyang District, Beijing, 100012, People's Republic of China
[7] CSIRO Space and Astronomy, P.O. Box 1130, Bentley WA 6102, Australia
[8] INAF—Osservatorio Astronomico di Cagliari, Via della Scienza 5, I-09047 Selargius, CA, Italy
[9] Instituto de Astrofísica de Andalucía (CSIC), Spain
[10] CSIRO Astronomy and Space Science, Australia Telescope National Facility, P.O. Box 76, NSW 1710, Australia
[11] School of Science, Western Sydney University, Locked Bag 1797, Penrith, NSW 2751, Australia
[12] Telethon Kids Institute, Perth Children's Hospital, Perth, Australia
[13] Argelander-Institut für Astronomie, Universität Bonn, Auf dem Hügel 71, D-53121 Bonn, Germany
[14] Aix Marseille Univ, CNRS, CNES, LAM, Marseille, France
[15] University of Louisville, Department of Physics and Astronomy, 102 Natural Science Building, Louisville, KY 40292, USA
[16] Department of Physics and Astronomy, Sejong University, 209 Neungdong-ro, Gwangjin-gu, Seoul 05006, Republic of Korea
[17] Royal Military College of Canada, P.O. Box 17000, Station Forces, Kingston, Ontario, K7K 7B4, Canada
Received 2021 November 1; revised 2021 December 2; accepted 2021 December 10; published 2022 March 4

Abstract

We study the tidal interaction of galaxies in the Eridanus supergroup, using H I data from the pre-pilot survey of the Widefield ASKAP *L*-band Legacy All-sky Blind surveY. We obtain optical photometric measurements and quantify the strength of tidal perturbation using a tidal parameter $S_{\rm sum}$. For low-mass galaxies of $M_* \lesssim 10^9\ M_\odot$, we find a dependence of decreasing H I to optical disk size ratio with increasing $S_{\rm sum}$, but no dependence of H I spectral line asymmetry with $S_{\rm sum}$. This is consistent with the behavior expected under tidal stripping. We confirm that the color profile shape and color gradient depend on the stellar mass, but there is an additional correlation of low-mass galaxies having their color gradients within $2R_{50}$ increasing with higher $S_{\rm sum}$. For these low-mass galaxies, the dependence of color gradients on $S_{\rm sum}$ is driven by the color becoming progressively redder in the inner disk when tidal perturbations are stronger. For high-mass galaxies, there is no dependence of color gradients on $S_{\rm sum}$, and we find a marginal reddening throughout the disks with increasing $S_{\rm sum}$. Our result highlights tidal interaction as an important environmental effect in producing the faint end of the star formation suppressed sequence in galaxy groups.

Unified Astronomy Thesaurus concepts: Galaxies (573); Interstellar atomic gas (833); Galaxy evolution (594); Galaxy environments (2029)

1. Introduction

Lambda cold dark matter (CDM) simulations predict that groups and clusters of galaxies started to assemble in large quantities from a redshift of ∼2 (e.g., Gao et al. 2004). By the present time, more than 20% of the galaxies with a stellar mass above $10^{10}\ M_\odot$ are likely satellites of groups (e.g., Zehavi et al. 2005; Croton et al. 2006), and the ratio increases for galaxies with lower stellar masses, up to 30% for galaxies with $M_* > 10^9\ M_\odot$ (e.g., van den Bosch et al. 2007; Yang et al. 2008). Thus the environment plays an increasingly important role in galaxy evolution at later epochs (e.g., van den Bosch et al. 2008; Wetzel et al. 2013; Haines et al. 2015). Theories and observations have converged on the point that galaxies grow primarily through forming stars, and the neutral hydrogen provides the raw material for forming stars (see, e.g., Bigiel et al. 2008). While molecular gas may be the more direct star-forming material, the H I, which can be further replenished by gas cooling and accretion from the circumgalactic medium (CGM), provides the reservoir to sustain the star formation (e.g., Saintonge et al. 2016; Catinella et al. 2018; Wang et al. 2020; Guo et al. 2021). Because of its low density and often extended nature, the H I is an excellent probe of environmental effects. Thus the variation of star formation rate (SFR) and H I richness in different environments with respect to those in the field is an effective measure of the effect of environment on galaxy growth (Boselli & Gavazzi 2006, 2014; Cortese et al. 2021).

Several observational trends have been established that serve as benchmarks of environmental effects in galaxy evolution models. The SFR and H I richness of galaxies tend to be lower in more massive groups (e.g., Kilborn et al. 2009; Hess & Wilcots 2013), and lower in satellites than in central galaxies (e.g., Fabello et al. 2012; Brown et al. 2017). For satellites, the

Original content from this work may be used under the terms of the Creative Commons Attribution 4.0 licence. Any further distribution of this work must maintain attribution to the author(s) and the title of the work, journal citation and DOI.

SFR and H I richness tend to be lower in the vicinity of group centers (e.g., Gavazzi et al. 2005, 2006), and at higher local densities (e.g., Gavazzi et al. 2013; Reynolds et al. 2020). These trends tend to be more prominent for low-mass galaxies than for high-mass galaxies (e.g., Boselli et al. 2014). These environmental trends are based on general parameters of the environment, which effectively capture but mix different physical mechanisms. For example, a high level of small-scale density can be related to tidal interaction events in a compact group, or harassments (Moore et al. 1996) in a cluster; a high level of large-scale density can be related to fly-by interactions (e.g., Mihos et al. 1992; Sinha & Holley-Bockelmann 2012) in a loose group, or ram pressure stripping (Gunn & Gott 1972) from the dense hot gas of a massive cluster. Even in a given cluster or group, weak ram pressure and tidal effects coexist near the virial radius (e.g., Balogh et al. 2000; Koopmann & Kenney 2004), while ram pressure stripping, viscous stripping (Nulsen 1982), evaporation (e.g., Nipoti & Binney 2007), harassment, and galaxy-cluster tidal effects coexist at intermediate cluster-centric radii. Moreover, those environmental parameters often ignore the infall trajectory of galaxies into the dense environment, which plays a crucial role in determining the relative importance of different environmental processes (e.g., Vollmer et al. 2001; Smith et al. 2015; Jackson et al. 2021).

Studies based on various galaxy samples have been designed to specifically investigate different gravitational or hydrodynamic processes. The galaxy–galaxy tidal interaction or merger, because of its prevalence in low- to intermediate-mass groups (e.g., Chung et al. 2009) and its strong link to starbursts (Larson & Tinsley 1978), has received extensive attention. These are typically based on samples of phase-space selected galaxy pairs (e.g., Lambas et al. 2003; Ellison et al. 2010) or morphologically selected post-mergers (e.g., Toomre & Toomre 1972). Whether and when the global SFR, the central SFR, and the SFR in the outer disks are boosted or quenched are key signatures that are frequently searched for. It was found that mergers or galactic interactions on average moderately and significantly elevate the total and central SFR of star-forming galaxies (e.g., Mihos & Hernquist 1994; Lisenfeld et al. 2007; Morales-Vargas et al. 2020; but see Martinez-Badenes et al. 2012 for the case in compact groups). The central and total SFR of the primary galaxy (the more massive one) is more strongly elevated if the interacting pair has a higher SFR, a higher stellar mass, a smaller separation, or a lower relative velocity (e.g., Zasov & Sulentic 1994; Alonso et al. 2004; Bustamante et al. 2018). The central SFR of the target galaxy may become suppressed if the interacting neighbor is passive, possibly due to a lack of a hydrodynamic interaction between the interstellar medium (ISM) of one galaxy with that of the other, and/or a ram pressure removal of the CGM by the dense CGM of the neighbor (e.g., Park & Choi 2005; Cao et al. 2016). The SFR in the outer disk may be temporarily suppressed alongside an elevated central SFR in the beginning of the interaction (e.g., Pan et al. 2019). There is also evidence that galactic interactions may fuel an active galactic nucleus (AGN; e.g., Sabater et al. 2008), destroy, induce, or strengthen bars (e.g., Barnes & Hernquist 1991, 1996), dilute metallicities (e.g., Kewley et al. 2010; Bustamante et al. 2020), heat the CGM (e.g., Cox et al. 2004), and modify the molecular gas mass (Lisenfeld et al. 2011, 2017). The SFR (distribution) and H I richness may be altered by these additional effects.

Theoretical studies suggest that tidal interactions affect the SFR level and distribution through modifying the cold gas distribution and kinematics, and the rate of converting cold gas to stars (e.g., Toomre & Toomre 1972; Cox et al. 2008; Hopkins et al. 2009). However, statistical studies of the response of the H I gas to tidal interactions has mostly been conducted with single-dish total H I fluxes (e.g., Ellison et al. 2015, 2018a). The total H I mass in post-mergers has been found not to be depleted but possibly slightly increased (e.g., Ellison et al. 2018a), raising the question of how galaxies managed to maintain little net change in H I richness, while there can be violent inflow and conversion of H I to fuel the AGN and star formation, with accompanying energetic feedback (e.g., Ellison et al. 2011; Hopkins et al. 2013). Studying the H I content of galaxy pairs is harder with single-dish observations, as their resolutions are usually not high enough to resolve the individual galaxies. Thus, some studies only investigated the total H I content of the system at different merger stages (e.g., Stierwalt et al. 2015; Zuo et al. 2018), while some others try to deblend the total H I into the individual galaxies based on their positions within the telescope beam and assumptions about their properties (e.g., Haynes et al. 2011; Bok et al. 2020). These studies consistently find that the H I richness of merging pairs remains normal with respect to isolated galaxies. But we caution that diffuse and extended H I tails produced in interactions can go beyond the single-dish beam or be resolved out in a targeted observation (e.g., For et al. 2019; Lee-Waddell et al. 2019). Such tails are prevalent, as demonstrated by interferometric H I images of a number of local compact groups (e.g., Verdes-Montenegro et al. 2001; Serra et al. 2013; Reynolds et al. 2019).

Although our knowledge about how galactic properties depend on local densities and how different types of tidal interactions modify galactic properties accumulates, a statistical quantification of how tidal interactions, among many other environmental mechanisms in the context of fully mapped groups/clusters, affect the SFR distribution and H I richness has been limited (e.g., Cortese et al. 2021). Considering the possible hydrodynamical effects additionally provided by the dense intracluster medium, it is important to separate the effects of tidal interactions from hydrodynamic effects in order to better understand the initial conditions of galaxies before they infall into and evolve in the groups/clusters (e.g., Wetzel et al. 2013). Previous results suggest that tidal enhancement of central SFR is much weaker in high-density regions than in low-density regions (Sol Alonso et al. 2006; Kampczyk et al. 2013). However, as passive galaxies are more abundant in dense environment, it is unclear whether this trend is more driven by the (lack of) ISM–ISM hydrodynamic effects (Ellison et al. 2010), or by other effects more related to the large-scale cluster properties (Perez et al. 2009).

The Eridanus supergroup, observed in the pre-pilot stage of the Widefield ASKAP *L*-band Legacy All-sky Blind surveY (WALLABY; Koribalski et al. 2020), provides us with an opportunity to study the galaxy–galaxy tidal effects in a complete cosmic structure. It consists of three groups undergoing a major merger into one cluster (Willmer et al. 1989; Omar & Dwarakanath 2005; Brough et al. 2006), which should increase the frequency of galactic tidal interactions with respect to isolated groups of similar masses (Fujita 1998; Gnedin 2003). Such systems should be more common at high redshift, but Eridanus is unique below a redshift of 0.08

(Burgett et al. 2004). Its proximity enables us to explore the behavior of the extremely low-mass ($M_* < 10^9\ M_\odot$) dwarf galaxies, which are building blocks of more massive galaxies, and more vulnerable to environmental effects than the massive galaxies. Simulations suggest that perturbation from even a minor neighbor with a mass ratio less than 1/10 could induce gas inflows (Hani et al. 2020; Patton et al. 2020). However, despite their significant tidal contribution, such low-mass dwarfs are often not included (e.g., Kauffmann et al. 2004) or suffer from incomplete sampling (e.g., Tortora et al. 2010) in Sloan Digital Sky Survey (SDSS) based studies due to the limited depth of SDSS images. With the availability of deeper and wider optical and radio data (e.g., WALLABY and Legacy Survey; see Section 3.1.1), we can build a more comprehensive picture of galaxy evolution across the spectrum of galaxy mass.

The moderate resolution of WALLABY is not sufficient to resolve the H I in all of the galaxies, but greatly helps deblend the H I emission that could have been confused in single-dish observations, as well as capture extended H I tails that could extend beyond a single-dish beam. A sample selected by H I flux can be biased against relatively gas-poor and passive galaxies, but is advantageous for focusing on the early stage of environmental processing. Such a selection is particularly useful to break the nurture or nature degeneracy encountered in environment studies, where gas-poor galaxies in dense environments can either reflect ongoing environmental processing or the cluster assembly history.

The paper is organized as follows. We introduce the samples that we construct and the data we use for our study in Section 2. We illustrate how we treat the data and derive physical parameters, including color gradients and tidal parameters, in Section 3. The results related to H I asymmetry, H I to optical disk size ratio, color profile, color gradients, and tidal parameters are presented in Section 4. Then in Section 5 we link our results to previous theoretical and observational studies and discuss the implications for group galaxy evolution. At last, in Section 6, we summarize the key results and the conclusions on our findings.

2. Sample

2.1. The H I Sample of WALLABY Detected Galaxies in the Eridanus Supergroup

The Eridanus supergroup was observed by the Australia Square Kilometre Array Pathfinder (ASKAP) as part of WALLABY (Koribalski et al. 2020) in its pre-pilot phase. With 36 antennas functioning, the data reach a detection limit of 2.4−4.4 mJy beam^{-1} across the field (central beams have a lower rms than the beams at the edge of the field) with a spatial resolution of 30″ and a channel width of 18.5 kHz, or 4 km s^{-1}. The raw data were reduced with ASKAPsoft (Whiting et al. 2020). The H I data cube was searched for detections with SoFiA (Serra et al. 2015; Westmeier et al. 2021). The products including velocities, coordinates, H I total fluxes, and moment maps, were released internally to the WALLABY team. More details about the data can be found in previous WALLABY publications studying the Eridanus fields (For et al. 2021; Murugeshan et al. 2021; Wong et al. 2021).

We exclude two H I clouds (H I detections with no optical counterparts): WALLABY J033911-222322 and WALLABY J033723-235753, which are studied in detail by Wong et al. (2021). The main purpose of this paper is to study how galaxies evolve in the Eridanus supergroup, so we select from the remaining 53 H I detections using the following criteria: (1) classification as a member of any of the three subgroups by Brough et al. (2006; Section 2.2), or (2) presence within the escape velocity curve and two virial radii in the phase-space diagram of any of the three subgroups. The mass, virial radius, and velocity dispersion of each group are taken from Brough et al. (2006). The selection results in 36 galaxies, which we refer to as the H I sample that serves as the main analysis sample. The radial velocities of galaxies in the H I sample range from ∼1200 to ∼2000 km s^{-1}.

We adopt a distance of 20.9 Mpc (Forbes et al. 2006) for the Eridanus supergroup. We take the SFR estimated in For et al. (2021) following the procedure described in Wang et al. (2017). In brief, each SFR is considered to be the sum of dust attenuated and unattenuated SFRs. The dust unattenuated SFR is estimated based on the Galaxy Evolution Explorer (GALEX; Martin et al. 2005) far-ultraviolet (FUV; near-ultraviolet, or NUV, when FUV is not available) luminosities, and the dust attenuated part of the Wide-field Infrared Survey Explorer (WISE; Wright et al. 2010) W4 luminosities. When neither FUV nor NUV data are available, the W4 SFR is taken as the lower limit of the total SFR. When there is no detection in the W4 band, zero dust attenuation is assumed.

2.2. The Optical Sample Combining the Brough et al. (2006) Catalog and Cosmicflows-3 Catalog

Brough et al. (2006) compiled a catalog of galaxies in the Eridanus supergroup combining data from 6dFGS, NED, and HyperLEDA. The flux limit is roughly 13.1 mag in the *K* band. They assigned in total 60 members to the three subgroups (NGC 1407 group, NGC 1332 group, and Eridanus group) of the supergroup using the friends-of-friends method. We exclude two galaxies (APMUKS(BJ) B033830.70-222643.7 and NGC 1331) from the supergroup members due to problematic optical images, and use the remaining 58 galaxies as the first part of our optical catalog.

Cosmicflows-3 (Tully et al. 2016) is the best existing description of the large-scale environment surrounding the Eridanus supergroup. We use the Cosmicflows-3 catalog to include nonmember galaxies near the edge of the supergroup that are not close enough to ensure a group membership, but are close enough to exert a significant tidal force on the relatively outlying group members. We do not use the member identification for the Eridanus supergroup itself from the Cosmicflows-3 group catalog (Tully 2015; Tully et al. 2016), because its galaxies were selected with a flux limit (11.75 mag in the *K* band) brighter than that of Brough et al. (2006), and so missed a large fraction of the WALLABY detected, H I-rich dwarf galaxies.

For each member galaxy of the Eridanus supergroup, we search for galaxies in the Cosmicflows-3 catalog that are within a projected distance of 0.8 Mpc around the member galaxy, and which differ in luminosity distance from the Eridanus supergroup center by less than 4.11 Mpc (three times the virial radius of the supergroup), but were not identified as members of the supergroup in Brough et al. (2006). By doing so, we select in total three galaxies, which is the second part of the optical catalog. Although the number of three looks small, this procedure confirms that we do not evidently miss an outlying population possibly contributing to the summed tidal strength that is not included by Brough et al. (2006). If we increase the

threshold projected distance to 1.37 Mpc (the virial radius of the supergroup), only five more galaxies are further included and these additional galaxies contribute less than 5% of the total tidal strength to any of the relevant galaxies in the H I sample. We thus stick to a threshold of 0.8 Mpc. Low-mass galaxies are largely missed by the Cosmicflows-3 catalog, but they contribute little to the total tidal forces as we will show later.

Finally, we have 61 galaxies in total in our optical sample. We retrieve radial velocities for optical sample galaxies from NED, by selecting the measurement in the optical with the minimum uncertainty. When no measurement is available, we take those labeled as "preferred" by NED. There are 22 galaxies from the H I sample that are overlapping with the optical sample. For these galaxies, we adopt the H I systematic velocities from WALLABY as their radial velocities.

3. Analysis

3.1. Photometry

3.1.1. Optical Total Fluxes and Surface Brightness Profiles

We use optical g, r, and z images from the DESI Legacy Survey (Dey et al. 2019) to derive photometric measurements for the two samples. The typical FWHM of the point-spread function is $1\farcs2$. The typical depths are 23.7, 23.3, and 22.2 mag in the g, r, and z bands, respectively.

We largely follow the photometry procedure of Wang et al. (2017). The main steps are described below.

1. *Deblending and masks.* We use SExtractor (Bertin & Arnouts 1996) to produce a mask image for each galaxy, through the so-called cold+hot source finding mode (e.g., Rix et al. 2004), based on the r-band image. In the cold mode, all clumps possibly belonging to the galaxy are merged into a master segmentation by setting the SExtractor deblending parameter to 0.3. Then, in the hot mode, small clumps in the master segmentation of the galaxy are picked out by setting the deblending parameter to 0.001. With the aid of the SExtractor output *CLASS_STAR*, we inspect the clumps in all three bands, so that foreground stars and background galaxies are masked. We then dilate the masks with a width of 11 pixels, to cover the scattered light of bright stars and galaxies. We inspect each masked image again, and adjust the mask when necessary.
2. *Galaxy shape and background subtraction.* We use SExtractor to derive the center, position angle, axis ratio, and a rough estimate of the background and background rms for each galaxy. We use the Python package *photutils* (Bradley et al. 2016) to derive a surface brightness profile in each of the three bands. The surface brightness is derived as the σ-clipped median value of pixels in elliptical rings, which have the center, position angle, and axis ratio fixed to the estimates of SExtractor. We identify the radius where the profile flattens within the noise level (the flattening radius hereafter), and use this part of the profile to estimate a local residual of the background. We remove this residual background from the radial profile. The uncertainty σ in the surface brightness values are calculated combining Poisson error and the uncertainties introduced in the two steps of background subtraction. We cut the radial profiles at the surface brightness level of 1σ.
3. *Clean image and total flux.* The pixels masked within the flattening radius are replaced by the surface brightness profile value at the corresponding radius. The pixels outside the flattening radius are assigned random values following a Gaussian distribution with a σ equivalent to the measured rms of the background. By doing so, we produce a clean image in each band for each galaxy. The clean images are inspected for quality. We finally run SExtractor again on the clean image to derive the half-light radius R_{50} and Petrosian magnitude measurements.

Galactic extinction is corrected based on the Planck 2013 dust model (Abergel et al. 2014) and the dust extinction curve of Cardelli et al. (1989).

3.1.2. Stellar Mass, H I Mass, and Disk Sizes

We estimate the stellar mass based on the Petrosian fluxes in the r and g bands. The r-band stellar mass-to-light ratio based on the $g-r$ color is calculated according to the equation of Zibetti et al. (2009). The stellar masses are then estimated according to the r-band luminosity and stellar mass-to-light ratio. Optical disk sizes are estimated as $R_{25,g}$ in the g band. We perform linear interpolation on g-band surface brightness profiles to derive the radius where the surface brightness reaches 25 mag arcsec^{-2}.

H I masses of galaxies in the H I sample are from For et al. (2021). For the optical-only galaxies (i.e., those in the optical sample but not in the H I sample), we still need their H I masses (as part of the total baryonic mass) in the calculation of tidal forces later. We approximate the H I masses to be zero for the optical-only galaxies that are covered but not detected in the WALLABY observations. The upper limits of the H I mass are no larger than 10% of the stellar mass of these galaxies, and thus the H I mass does not contribute much to the total baryonic mass. We also confirm that the results are not changed if we assume the upper limits for the H I mass instead of zero.

For the optical-only galaxies beyond the WALLABY observing footprint (16 galaxies), we test two sets of approximations for the H I mass. In the first set, we approximate the H I mass to be zero, which leads to a lower limit of the baryonic mass of the galaxy. In the second set, we estimate the H I mass based on the $g-r$ color and effective stellar surface density, following the equation of Zhang et al. (2009). The second set of approximations can be viewed as an upper limit of H I mass, because the equation of Zhang et al. (2009) is derived using a sample that is strongly biased toward H I rich field galaxies (i.e., a cross match of the SDSS DR4 and HyperLeda H I data), while the galaxies in the optical sample are in a denser environment and tend be more H I deficient (For et al. 2021). We examine the final results based on the two types of approximations and do not find a significant difference. We thus use the H I masses estimated from color and surface density for the optical-only galaxies that are not in the WALLABY footprint.

We estimate the H I disk size $R_{\rm H\,I}$, the radius where the H I surface density reaches 1 $M_\odot$ pc^{-2} (Broeils & Rhee 1997), based on the size–mass relation of Wang et al. (2016). We do not directly derive $R_{\rm H\,I}$ from the WALLABY images for H I sample galaxies, because most H I disks in the H I sample are barely resolved. We confirm that the resolved disks are quite consistent with the H I size–mass relation with a scatter of 0.07 dex for the deviation.

3.1.3. Color Gradients for the H I Sample

Based on the surface brightness profiles, we derive color profiles and color gradients. We derive $g-r$, $g-z$, and $r-z$, but will focus on the $g-r$ color after finding that the trends are similar. The color uncertainty at each radius is calculated as $\sigma_{g-r}=\sqrt{\sigma_g^2+\sigma_r^2}$, where σ_g and σ_r are the errors of surface brightness in the g and r band, respectively. We limit color profiles to the radial range where $\sigma_{g-r}<0.1$ mag.

MacArthur et al. (2004) found that different fitting ranges for color gradients change the result, with flips in the sign of the color gradient within or beyond the effective radius (see also Bakos et al. 2008). Using integral field spectrograph facilities such as CALIFA and MaNGA, Marino et al. (2016) and Zheng et al. (2017) also found evidence of bending or breaks in color profiles of late-type galaxies. Thus, in this paper, color gradients are derived in two different radial ranges: $0<R<R_{50,z}$ and $R_{50,z}<R<2R_{50,z}$, which are denoted as CG_{01} and CG_{12}, respectively. We divide galaxies into pieces by $R_{50,z}$ instead of the break radius in color profiles, because it better traces the fractional growth of the stellar disk. At a radius of $2R_{50,z}$, 80% (90%) galaxies in our sample have the surface brightness in the r band brighter than 23.8 (24.5) mag arcsec^{-2}; thus restricting the analysis within this radius minimizes contamination from scattered light of neighboring galaxies or bright stars.

The color gradient (CG) is derived as the slope of the linear fit to the color profile $g-r$ as a function of $R/R_{50,z}$ in a given radial range, where R is the radius, and $R_{50,z}$ is the half-light radius in the z band. Specifically, the CG is given as $\mathrm{CG}=\delta(g-r)/\delta(R/R_{50,z})$. We use $R_{50,z}$ instead of other bands for it traces the stellar mass more closely, and has better signal-to-noise ratio than the half-M_* radius. We experiment with conducting the analysis throughout this paper based on the half-light radius in other bands and also based on the half-M_* radius, and the results do not significantly change and the correlations do not become stronger.

We point out that, when deriving the CG in the way described above, we have treated the galaxy as a whole. But the bulges should response less sensitively than disks to environmental effects, as the stars are older and hotter (e.g., Sandage & Bedke 1994). It will perhaps be useful in future studies to conduct bulge-disk decomposition and derive CG for disks only. However, as the $R_{90,z}/R_{50,z}$ value ranges from 1.9 to 2.8 (10th to 90th percentiles) in our sample, the influence of bulges on our results should not be severe.

3.2. Tidal Strength for the H I Sample

We use the tidal parameter suggested by theoretical studies to quantify the instantaneous tidal perturbation experienced by a galaxy. One of the commonly used parameters is the dimensionless tidal parameter $S_0=\left(\frac{M_p}{M_g}\right)\left(\frac{R_g}{d_{\rm peri}}\right)^3\left(\frac{\Delta t}{T}\right)$; (Oh et al. 2008), where M_p is the mass of the perturbing object, M_g is the mass of the galaxy of interest, R_g is the radius of the galaxy, and $d_{\rm peri}$ is the pericenter distance between the perturbing object and the galaxy. Term Δt is the time elapsed for the perturbing object to move over 1 radian near the pericenter, and $T\equiv\sqrt{\frac{R_g^3}{GM_g}}$ is the time taken by a test mass at $R=R_g$ to rotate 1 radian about the galaxy center. One obvious limitation with the S_0 parameter is that it does not apply to mergers in the coalescence stage where the gravitational effect is strong but the perturber is blended with the galaxy of interest. However, from inspecting the optical and H I images of the H I sample, there is only one system (NGC 1359, ID 69) clearly identified to be in the coalescence stage of a merger. We do not exclude this system, but discuss its potential contamination of the results when necessary.

In order to derive the parameter with observables, we make a few approximations. We use the projected distance ($d_{\rm proj}$) to approximate the pericentric distance and use $\frac{V_{\rm circ}/R_g}{\Delta v_{\rm rad}/d_{\rm proj}}$ to approximate $\frac{\Delta t}{T}$, where $V_{\rm circ}$ is the circular velocity of the galaxy, and $\Delta v_{\rm rad}$ is the difference in line-of-sight velocity of the two objects. In addition, we add a smooth parameter $V_{\rm smooth}$ to $\Delta v_{\rm rad}$ to avoid zero divides. By adding the smooth parameter we artificially set a lower limit to the relative line-of-sight velocity between any two galaxies. We use a fiducial value of $V_{\rm smooth}=V_{\rm circ}$, which ranges from $\sim$50 to $\sim$180 km s^{-1} and has a median of $\sim$80 km s^{-1}, but also tried other options including 50, 100, and 200 km s^{-1}. We confirm that all of the major trends in Section 4 do not significantly change unless $V_{\rm smooth}$ is set to unrealistically small values, such as 10 km s^{-1}.

The derived dimensionless tidal parameter is thus calculated as

$$S=\left(\frac{M_p}{M_g}\right)\left(\frac{R_g}{d_{\rm proj}}\right)^2\left(\frac{V_{\rm circ}}{\sqrt{(\Delta v_{\rm rad})^2+V_{\rm smooth}^2}}\right). \quad (1)$$

Such approximations have obvious uncertainties. Consider the case in which $V_{\rm smooth}=0$. First, the projected quantities $d_{\rm proj}$ and $\Delta v_{\rm rad}$ are the lower limits of the real separation (d) and velocity difference (Δv) between the galaxy and the perturber, so $\left(\frac{1}{d_{\rm proj}}\right)^2(\frac{1}{\Delta v_{\rm rad}})$ is an overestimate of $\left(\frac{1}{d}\right)^2(\frac{1}{\Delta v})$. That said, the real separation and velocity difference are upper and lower limits of the distance and rotational velocity ($d_{\rm peri}$ and $v_{\rm peri}$, respectively) of the perturber at the pericenter. If we assume the angular momentum to be conserved in the frame centered on the galaxy, $d_{\rm peri}v_{\rm peri}=d\Delta v\equiv$ const, then $\left(\frac{1}{d}\right)^2(\frac{1}{\Delta v})$ is an underestimate of $\left(\frac{1}{d_{\rm peri}}\right)^2(\frac{1}{\Delta v_{\rm peri}})$. As a result, depending on circumstances the observationally derived S can either underestimate or overestimate the physical S_0. So S should only be viewed as a statistically correct indicator of S_0, and its relevant analysis should only be interpreted in a statistical sense. We roughly quantify the uncertainty of S by using the velocity dispersion of Eridanus supergroup galaxies ($\sigma=265$ km s^{-1}; Willmer et al. 1989) as the relative line-of-sight velocity $\Delta v_{\rm rad}$. We estimate a typical error of 0.3 dex for each perturber −perturbed object pair.

In addition, the infall history of the galaxies also introduces a physical uncertainty. The tidal effect is strongest when galaxies are at pericenter. For galaxies that have already gone past that, the instantaneous measure of tidal strength, i.e., the tidal parameter, may underestimate the persistent effect of tidal interaction. Therefore, the tidal parameter may be regarded as a lower limit of the real effect. However, our sample is biased against galaxies that are at pericenter, since their velocities there are then the highest, and thus the time elapsed is the shortest. But this last limitation generally applies to all randomly selected samples.

Despite these uncertainties, we point out that the estimate of the S parameter is observationally supported by previous findings of tidally induced galactic features (e.g., enhanced central star formation, more perturbed optical disk morphologies) being correlated with the mass ratio, projected distance, and radial velocity offset of galaxy pairs separately (Alonso et al. 2004; Ellison et al. 2010; Bustamante et al. 2018; Pan et al. 2018). The use of the S parameter combines these dependent factors in a physically motivated way, and avoids addressing the degeneracy between these factors when investigating the dependence of other galactic properties on the tidal strength. The latter point is particularly important for this study as the sample is not very large. In the following, we describe the derivation of $V_{\rm circ}$, and our options for R_g and masses (M_p and M_g).

3.2.1. Estimation of Total Mass

We calculate the baryonic mass as $M_b = M_* + 1.4M_{\rm H\,I}$. The rotational velocity $V_{\rm circ}$ is estimated using the baryonic Tully−Fisher relation of McGaugh et al. (2000). We do not directly derive $V_{\rm circ}$ from the WALLABY data cube because only a small fraction of the galaxies are spatially resolved. We do not derive $V_{\rm circ}$ from the width of the global H I profile either, because the integral line width may not well trace $V_{\rm circ}$ when galaxies are perturbed (e.g., Reynolds et al. 2020; Watts et al. 2020a, 2020b). Furthermore, a significant fraction of galaxies in the H I sample are dwarf irregular galaxies, which in the optical tend to have thick disks and an uncertain axis ratio due to the irregular morphology (e.g., Sánchez-Janssen et al. 2010; Oman et al. 2019). Thus deriving the inclination angle and deprojecting the global line widths are expected to have large uncertainties.

The total mass enclosed by radius R is calculated as $M = M(R) = V_{\rm circ}^2 R/G$, where G is the gravitational constant, and R should be large enough to be roughly in the regime where the rotation curve reaches $V_{\rm circ}$. At this point, we have three options for R: the optical radius $R_{25,g}$, the H I radius $R_{\rm H\,I}$, and the baryonic radius R_b, which is the larger of $R_{25,g}$ and $R_{\rm H\,I}$. Directly referring to the theory of tidal interaction, masses (and thus tidal parameters) estimated with $R_{25,g}$ ($R_{\rm H\,I}$) should be more sensitive probes of perturbations to the stellar (H I) disk, while tidal parameters estimated using R_b should be a more general indicator of whether the galaxy is perturbed. We take the mass (and thus the tidal parameter) estimated with $R_{25,g}$ as the fiducial measure, for in the analysis later we mainly focus on the effect of tidal interactions on the optical color gradients. But we reiterate that, if we change to R_b or $R_{\rm H\,I}$, our major conclusions are not affected.

3.2.2. Tidal Strength from Different Perturbers

We use the term "perturber" to refer to the galaxy that causes tidal perturbation on the galaxy of interest. For each galaxy in the H I sample, the perturbers come from the superset combining the H I sample and the optical sample (75 galaxies altogether). We estimate the strength of tidal perturbation caused by each perturber, S_i, where i denotes the specific perturber.

Strengths of tidal perturbation caused by perturber(s) are estimated in three ways as follows:

1. That which is caused by the nearest perturber ($S_{\rm nearest}$). The nearest perturber is defined as the one that has the smallest projected angular distance to the galaxy.
2. That which reflects the most severe perturbation caused by any perturber ($S_{\rm strongest}$), i.e., $S_{\rm strongest} = \max(S_i)$.
3. That which reflects the summed effect of perturbation caused by all of the perturbers ($S_{\rm sum}$). Mathematically, $S_{\rm sum} = \Sigma_i S_i$, where i denotes different perturbers, and it is referred to as "the summed tidal parameter" in the following.

From first principles, tidal forces are vectors. However, when quantifying the cumulative tidal effects on a galaxy, it is not straightforward to treat the observables as vectors. For example, even when the instantaneous tidal forces from several companions cancel out as vectors at a given time, the cumulative tidal effects from these companions do not necessarily do so. This is because the orbits of the companions during one rotation period of the subject galaxy do not always cancel out. Based on such consideration, we consider $S_{\rm sum}$ in addition to $S_{\rm strongest}$ and $S_{\rm nearest}$ in our analysis. Both the scalar sum (e.g., Argudo-Fernández et al. 2015) and strongest (e.g., Karachentsev et al. 2013) tidal strengths were calculated in the literature to quantify the tidal fields. We find consistent results in most cases, but in some cases, $S_{\rm sum}$ shows a stronger correlation with galactic properties (e.g., $\rm CG_{01}$ and $R_{\rm H\,I}/R_{25,g}$; see Sections 4.4 and 4.2), implying that $S_{\rm sum}$ is a more complete indicator of the total tidal effects (but not tidal forces) felt by a galaxy.

The key results of this study do not significantly change if we use other parameters such as $\Theta \equiv \log[(M_*/10^{11}M_\odot)(d_{\rm proj}/{\rm Mpc})^{-3}]$ as the measurement of tidal strength (e.g., Karachentsev et al. 2013; Pearson et al. 2016; Wong et al. 2021).

3.2.3. Significant Contributors of the Summed Tidal Strength

We investigate how many galaxies significantly contribute to the summed tidal strength ($S_{\rm sum}$) and their spatial distribution for each galaxy. We use the curve of growth to analyze how the cumulative tidal strength increases as more neighbors are considered. For each galaxy, we first rank its perturbers by order of decreasing tidal strength, and calculate the cumulative sum. Then we normalize the cumulative tidal strengths by the summed tidal strength $S_{\rm sum}$. The number of galaxies that contribute to 80% of $S_{\rm sum}$ is then determined by the curves of growth, and is denoted as N_{80}. To illustrate the spatial distribution of these significant contributors, we further determine D_{80}, which is the maximum distance between them and the subject galaxy. We also obtain the distances between the nearest (strongest) perturber and the subject galaxy as $D_{\rm nearest}$ ($D_{\rm strongest}$). To quantify how important low-mass perturbers are, we also calculate the part of $S_{\rm sum}$ that is contributed by perturbers with a stellar mass lower than $10^9\,M_\odot$, which we denote as $S_{{\rm sum},M_*<10^9M_\odot}$.

We divide the subject galaxies by the 75th percentile value of $\log S_{\rm sum} = -1.69$ to separate them into two groups, hereafter strongly perturbed galaxies and weakly perturbed galaxies. The weakly perturbed galaxies are expected to have larger D_{80} and N_{80} than the strongly perturbed galaxies under similar circumstances, which is confirmed by our results. As can be seen in Figure 1, the ellipses of D_{80} are larger than those of $D_{\rm strongest}$ and $D_{\rm nearest}$ in most cases of strongly perturbed ($\log S_{\rm sum} > -1.69$) galaxies. This suggests that $S_{\rm sum}$ has a

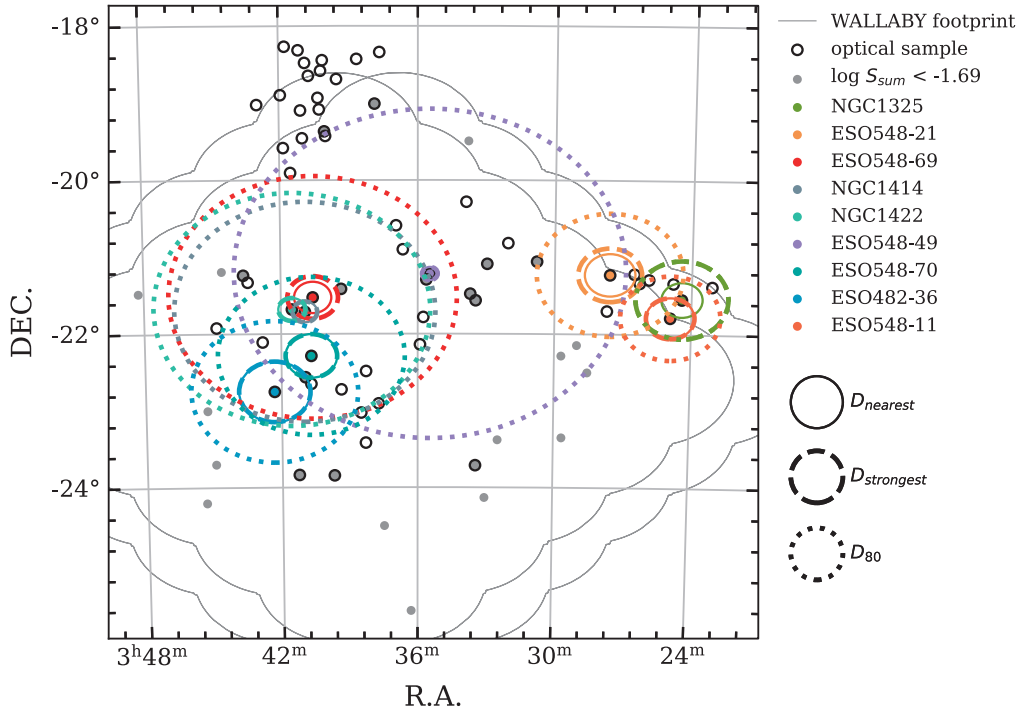


Figure 1. The spatial distribution of galaxies in the H I and optical samples. Black open circles are galaxies from the optical sample, while filled circles are those from H I sample. Among the H I sample galaxies, strongly perturbed galaxies (i.e., those with $\log S_{\rm sum} > -1.69$) are presented in colors (see labels on the right) and weakly perturbed galaxies are plotted in gray. D_{80} (dotted-line ellipses), $D_{\rm strongest}$ (dashed-line ellipses), and $D_{\rm nearest}$ (solid-line ellipses) of nine strongly perturbed galaxies are presented in the same color as the subject galaxy. In many cases, the dashed ellipse overlaps with the solid ellipse. The shape of the two WALLABY Eridanus footprints are shown by light gray lines. Note that NGC 1325 has equal $D_{\rm strongest}$ and D_{80}.

significant contribution from perturbers over a relatively large distance range, even though in some cases D_{80} is only ∼2 times $D_{\rm nearest}$. It can also be seen that the strongest perturber is usually the nearest perturber, but not always, as indicated by the frequent overlapping of dashed- and solid-line ellipses. The difference between $D_{\rm nearest}$, $D_{\rm strongest}$, and D_{80} for strongly perturbed galaxies is more clearly illustrated in the lower-left panel of Figure 2. Most (90%) of the strongly perturbed galaxies have D_{80} larger than 0.3 Mpc, but $D_{\rm strongest}$ never exceeds this value.

We show in the upper-left panel of Figure 2 the curves of growth of tidal strength for individual strongly perturbed ($\log S_{\rm sum} > -1.69$) galaxies and the median trend. In the median, four galaxies contribute 80% of $S_{\rm sum}$. For individual strongly perturbed galaxies, N_{80} ranges from 2 to 7. In the upper-right panel of Figure 2, we present the distribution of N_{80} for both strongly and weakly perturbed galaxies. Strongly perturbed galaxies do have smaller N_{80} compared to the weakly perturbed galaxies. Most (80%) galaxies have $N_{80} \geqslant 5$ and the whole sample has a median N_{80} of 7.

These results consistently suggest that the summed strengths of tidal perturbation experienced by the galaxies in the Eridanus supergroup come from a number (≳4) of their neighbor galaxies at larger distances (≳0.3 Mpc), rather than only the closest neighbors as is the case in close galaxy pairs or triplet systems in an isolated environment (e.g., Hibbard et al. 2001; Vollmer et al. 2005; Argudo-Fernández et al. 2014). Thus, investigating the tidal effects on group galaxies likely requires a complete sample covering a large enough sky area. Fortunately, the Eridanus supergroup is close by, and our wide-field WALLABY data help verify the completeness of redshifts for the gas-rich, low-mass galaxies. As we show in the lower-right panel of Figure 2, the low-mass ($M_* < 10^9\ M_\odot$) galaxies have a median contribution of ∼4% (∼7% for strongly perturbed galaxies) of $S_{\rm sum}$ and only 6 out of 36 galaxies have a fraction ≳20%. This result implies that $S_{\rm sum}$ is not significantly underestimated due to the K-band flux limit of the either the Brough et al. (2006) catalog or the Cosmicflow-3 catalog.

3.3. Additional Parameters

In addition to direct measurements of SFR and H I mass ($M_{\rm H\,I}$), we also use specific star formation rate (sSFR ≡ SFR/M_*), H I gas fraction ($f_{\rm H\,I} \equiv M_{\rm H\,I}/M_*$), deviation of SFR from the star-forming main sequence (ΔSFR ≡ log SFR − log $\rm SFR_{SFMS}(M_*)$, where $\rm SFR_{SFMS}(M_*)$ is the SFR expected for a typical star-forming galaxy at a given M_*; Saintonge et al. 2016), and deviation of H I mass from the median relation of $M_{\rm H\,I}$ versus M_* ($\Delta M_{\rm H\,I} \equiv \log M_{\rm H\,I} - \log M_{\rm H\,I,med}(M_*)$, where $M_{\rm H\,I,med}(M_*)$ is the median $M_{\rm H\,I}$ expected for galaxies of given M_*; Catinella et al. 2018).

Another parameter we use is the H I spectral line asymmetry ($A_{\rm spec}$). It is calculated following the procedure of Reynolds et al. (2020). $A_{\rm spec} \equiv \Sigma_i |S(i) - S_{\rm flip}(i)| / \Sigma_i |S(i)|$ is the normalized sum of the difference in flux intensity between the flipped spectrum and the original one, where $S(i)$ and $S_{\rm flip}(i)$ are the flux intensities in channel i of the original and flipped spectrum, respectively.

4. Results

Our analysis focuses on the H I sample. We separate the sample into low-mass and high-mass subsamples by the median value of stellar mass $M_* = 10^{8.95}\ M_\odot$. The division is chosen to maximize the statistics for both subsamples, and theoretically and observationally it roughly divides two distinct

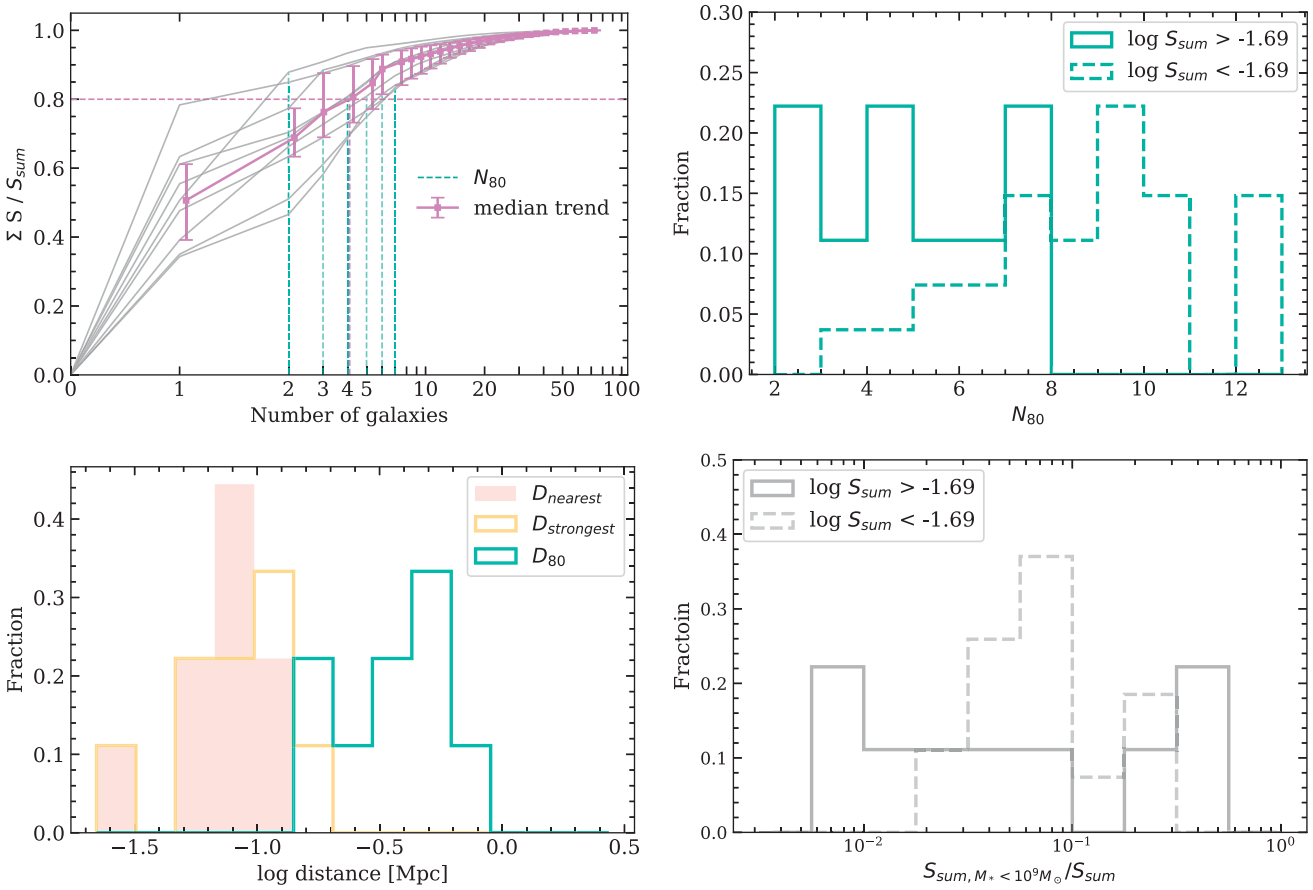


Figure 2. Properties of contributors to $S_{\rm sum}$. Upper left: the curves of growth for individual strongly perturbed galaxies (those with $\log S_{\rm sum} > -1.69$, in gray). The median value and scatter (25th and 75th percentiles) of the gray curves are shown in magenta. The N_{80} of individual (median) curves are labeled by vertical dashed cyan (magenta) lines. Upper right: the distribution of N_{80} for strongly perturbed ($\log S_{\rm sum} > -1.69$, cyan solid) and weakly perturbed ($\log S_{\rm sum} < -1.69$, cyan dashed) galaxies. Lower left: the distribution of $D_{\rm nearest}$ (pink), $D_{\rm strongest}$ (yellow), and D_{80} (cyan) for nine strongly perturbed galaxies. Lower right: the distribution of the fraction of $S_{\rm sum}$ that is contributed by perturbers with a stellar mass smaller than $10^9\ M_\odot$ ($S_{{\rm sum},M_*<10^9M_\odot}/S_{\rm sum}$; see text), for strongly perturbed (gray solid) and weakly perturbed (gray dashed) galaxies.

regimes of galaxy formation. A stellar mass of $\sim 10^9\ M_\odot$ corresponds roughly to a dark matter halo mass of $10^{11}\ M_\odot$ and virial velocity of $\sim 70\ {\rm km\ s^{-1}}$ (Behroozi et al. 2019). Thus galaxies with $M_* < 10^9\ M_\odot$ tend to be strongly affected by stellar winds and winds launched by supernova, which typically have speeds of the order of $100\ {\rm km\ s^{-1}}$ (e.g., Veilleux et al. 2005). Previous observational studies showed that galaxies with a stellar mass above and below this threshold indeed tend to have distinct $g-i$ color gradients (Tortora et al. 2010), disk thicknesses (Sánchez-Janssen et al. 2010), and slopes of the H I mass versus stellar mass relations (Maddox et al. 2015). We point out that, $\sim 10^9\ M_\odot$ is also approximately the lower limit of M_* for M_*-complete samples selected from SDSS (York et al. 2000) and the upper limit of M_* for dwarf irregular galaxies studied in the Local Volume in surveys such as LITTLE THINGS (Hunter et al. 2012).

We quantify the linear correlation strength with the Pearson R value ($|R| > 0.45$ as significant and $0.3 < |R| < 0.45$ as considerable) and the p-value of 5% significance. The uncertainties in the coefficients are calculated via bootstrapping. Given the sample size, an R value of 0.45 is roughly equivalent to a p-value of 0.05 for the correlation. When SFR is involved, we use the astronomical survival analysis (Feigelson & Nelson 1985; Isobe et al. 1986; Lavalley et al. 1992) rather than R to account for the lower limits. The Python package *pymccorrelation* and Kendall's τ model is used. We also perform a robust linear fit to the data points, and use the deviation of the slope from zero as a measure of the significance of a linear relation. We investigate the dependence of galactic properties on the three types of tidal strength parameters ($S_{\rm nearest}$, $S_{\rm strongest}$, and $S_{\rm sum}$). We present Pearson correlation coefficients for dependences on these three tidal parameters separately, but only show figures for trends related to $S_{\rm sum}$.

4.1. H I Asymmetry

The correlations between H I spectral asymmetries ($A_{\rm spec}$) and the summed tidal parameter ($S_{\rm sum}$) are presented in Figure 3. We do not find statistically significant evidence for a correlation between H I spectral asymmetries and tidal strength for either low-mass (left panel) or high-mass (right panel) galaxies. It indicates that, if high $S_{\rm sum}$ values are related to stronger perturbations, they are not reflected in the $A_{\rm spec}$ parameter. We remind the reader that $A_{\rm spec}$ values are measured from the integral spectra, and thus could miss local signatures of perturbation in the H I disks. It will be interesting to investigate how the multidimensional asymmetry is affected when better-resolved H I images are available in the future.

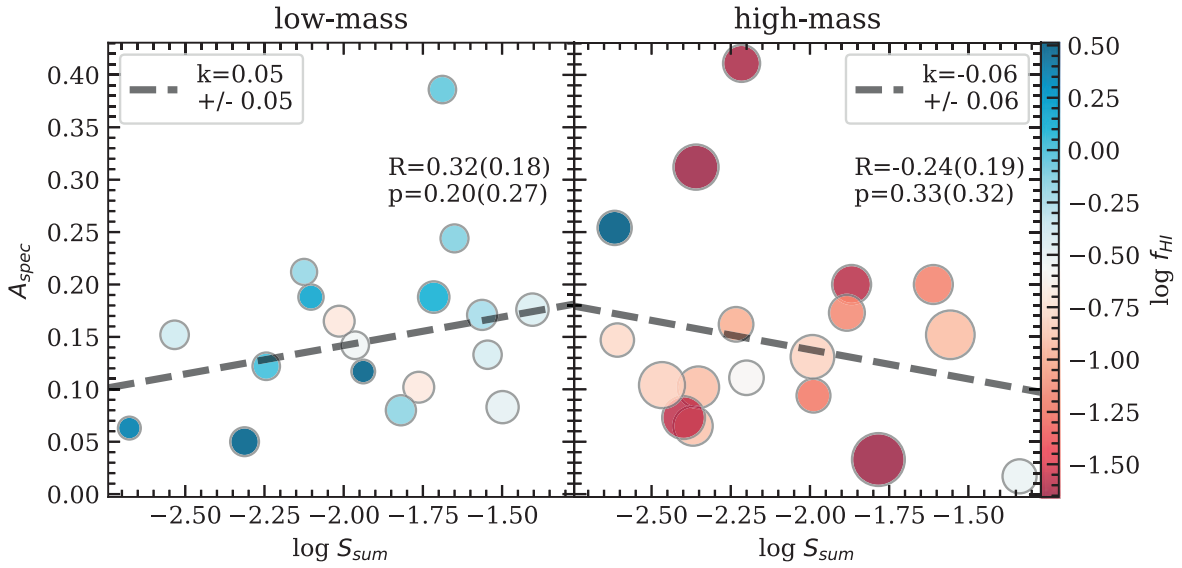


Figure 3. The correlation between H I spectral line asymmetry and the summed tidal parameter. Left: for low-mass ($\log M_*/M_\odot < 8.95$) galaxies. Right: for high-mass ($\log M_*/M_\odot > 8.95$) galaxies. Pearson R and p-values are shown with bootstrap errors in parentheses. Gray dashed lines are the results of a robust linear fit, with the slopes (and errors) shown in the corner. All data points are color coded by H I gas fraction (see color bar on the right). The size of data points indicates the stellar mass of the galaxy, in the sense that larger data points are used for more massive galaxies.

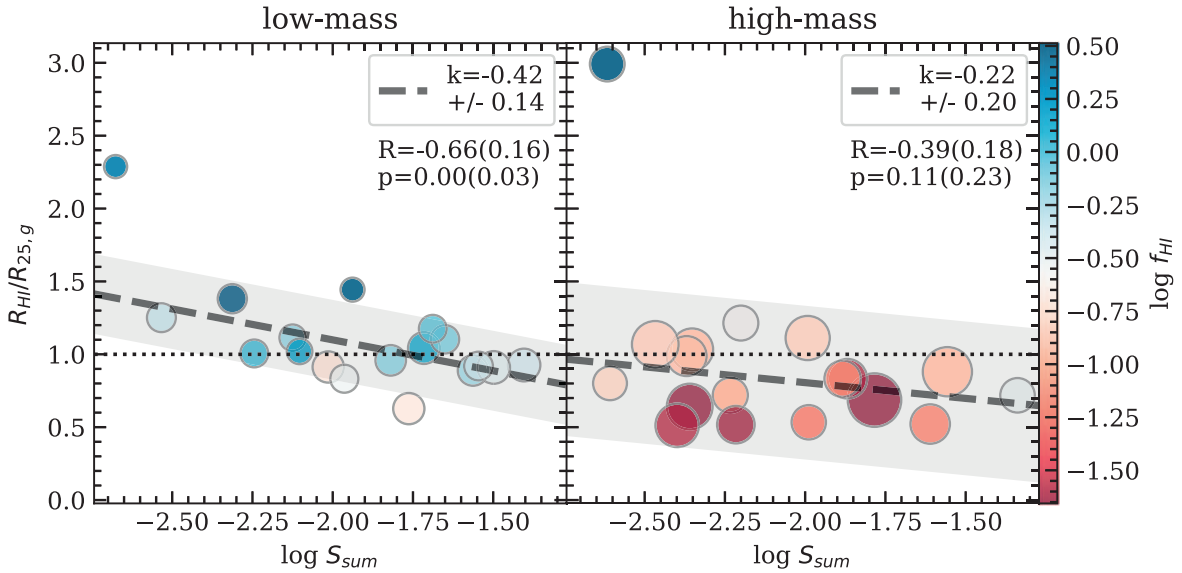


Figure 4. The correlation between the H I to optical disk size ratio and the summed tidal parameter. The gray shaded area indicates the scatter (1σ) of data points about the linear fit. The dotted horizontal line represents $R_{\rm H\,I}/R_{25,g} = 1$. Left: for low-mass ($\log M_*/M_\odot < 8.95$) galaxies. Right: for high-mass ($\log M_*/M_\odot > 8.95$) galaxies. The other symbols and text are the same as in Figure 3: Pearson R and p-values are shown with bootstrap errors in parentheses. Gray dashed lines are the result of a robust linear fit, with the slopes (and errors) shown in the corner. All data points are color coded by H I gas fraction (see color bar on the right). The size of data points indicates the stellar mass of the galaxy, in the sense that larger data points are used for more massive galaxies.

4.2. H I Disk Size

In Figure 4, we show the connection between the H I to optical disk size ratio ($R_{\rm H\,I}/R_{25,g}$) and $S_{\rm sum}$. Although $R_{\rm H\,I}$ is derived from H I mass and $R_{25,g}$ is strongly correlated with stellar mass, using the H I to optical disk size ratio instead of the H I to stellar mass ratio more directly traces the potential outside-in shrinking of H I disks with respect to the optical disks as a result of tidal perturbation.

The disk size ratios anticorrelate significantly with tidal strength in the low-mass sample. Most of the low-mass galaxies reside close to the best-fit linear relation except for LEDA 792493 (ID 63, in the upper-left corner) which has the lowest $S_{\rm sum}$ and highest size ratio of the low-mass subsample. LEDA 792493 is a relatively unperturbed, H I rich dwarf galaxy. If we exclude LEDA 792493 from this analysis, we obtain an R value of −0.47 and a p-value of 0.06. For high-mass galaxies, there is no significant correlation between disk size ratio and $S_{\rm sum}$. The best-fit linear relation has a larger scatter than that of low-mass galaxies, implying additional drivers for H I disk sizes in high-mass galaxies. The outlier NGC 1359 (ID 69) has the lowest $S_{\rm sum}$ and highest size ratio of the high-mass subsample. NGC 1359 is a merger system in the stage of coalescence. Because the whole system is treated as one galaxy, tidal strength $S_{\rm sum}$ only considers the perturbation from galaxies outside this system. The correlation coefficient between $S_{\rm sum}$ and $R_{\rm H\,I}/R_{25,g}$ for the high-mass galaxies becomes consistent with zero if NGC 1359 is excluded from the subsample.

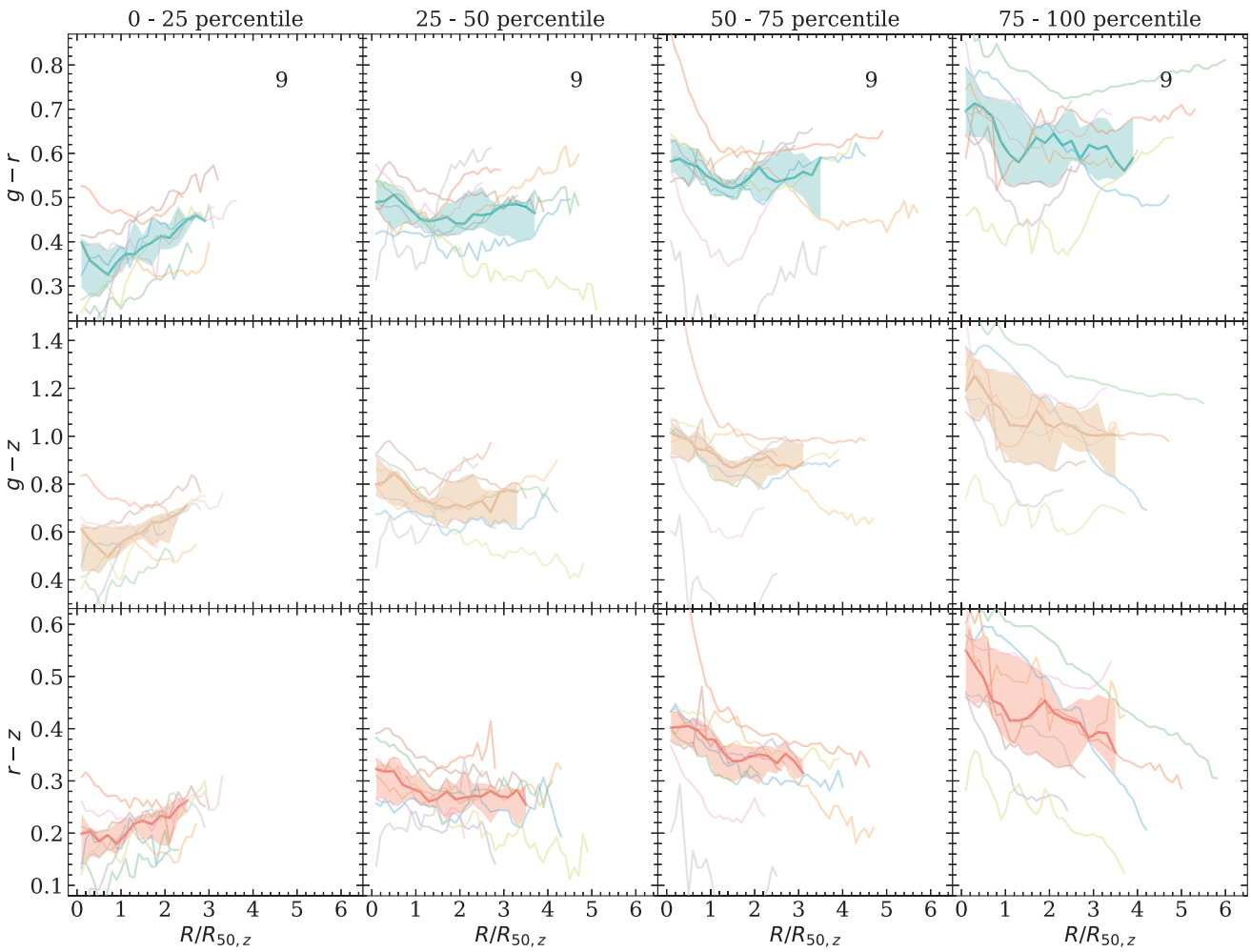


Figure 5. Color profiles in different stellar mass bins. From left to right: $7.5 < \log M_*/M_\odot < 8.43$, $8.43 < \log M_*/M_\odot < 8.95$, $8.95 < \log M_*/M_\odot < 9.5$, and $9.5 < \log M_*/M_\odot < 10.6$ (corresponding to 0th–25th, 25th–50th, 50th–75th, 75th–100th percentiles). From top to bottom: $g - r$ (green), $g - z$ (yellow), and $r - z$ (red). The color profiles for individual galaxies in each stellar mass bin are presented in random light colors. The median value and scatter (25th and 75th percentiles) of the individual profiles are shown in the dark color. The number of galaxies in each stellar mass bin is shown at the top.

Considering that $R_{25,g}$ may only enclose a small fraction of the total flux for the low-mass galaxies, we test by replacing it with four times the disk scale length ($4R_d$). We derive R_d by fitting the outer part of the surface brightness profile of the galactic disks in the g band. There is no qualitative difference between the results obtained by adopting $R_{25,g}$ and $4R_d$ as the disk size estimates (see section A.1 in the Appendices). We note that potential systematic uncertainties in the H I fluxes of the ASKAP data of Eridanus (For et al. 2021) only slightly shift (by a maximum of ∼0.09 dex) but do not affect the tightness of the trend.

4.3. Color Profiles

We investigate the overall shape of color profiles for galaxies of different stellar mass ranges. We divide the H I sample evenly into four subsamples by stellar mass. We show three types of color profiles ($g - r$, $g - z$, and $r - z$) in Figure 5. The profiles are radially normalized by the z-band half-light radius ($R_{50,z}$). The median profile of each subsample is calculated in the radial range where at least half of the galaxies have color uncertainties lower than 0.1 mag.

For the least-massive galaxies ($7.5 < \log M_*/M_\odot < 8.43$, 0th–25th percentile), the colors become redder almost monotonically toward large radius. For galaxies that have intermediate stellar masses ($8.43 < \log M_*/M_\odot < 8.95$ and $8.95 < \log M_*/M_\odot < 9.5$, 25th–50th and 50th–75th percentiles), the median profiles are almost flat and sometimes show a "U"-shape. For the most massive galaxies in our sample ($9.5 < \log M_*/M_\odot < 10.6$, 75th–100th percentile), the color profiles generally become bluer toward large radius. We checked the profiles after excluding mergers, i.e., NGC 1359 and NGC 1385 (ID 69 and ID 70), but see no significant change compared to that presented above.

4.4. Color Gradients

We study the relation between color gradients and $S_{\rm sum}$. Color gradients are commonly used to indicate whether stellar disks grow or stop growing inside-out or outside-in (e.g., Muñoz-Mateos et al. 2007; Wang et al. 2011; Pan et al. 2015, 2016). We focus on the $g - r$ color hereafter as the other two colors show similar patterns. Regarding the nontrivial shape of color profiles shown in Figure 5, we do not derive one single global color gradient for each galaxy. We consider color gradients calculated in different radius ranges, $0 < R < R_{50,z}$ and $R_{50,z} < R < 2R_{50,z}$, respectively, to better probe the variations in response to tidal perturbation. As before, the

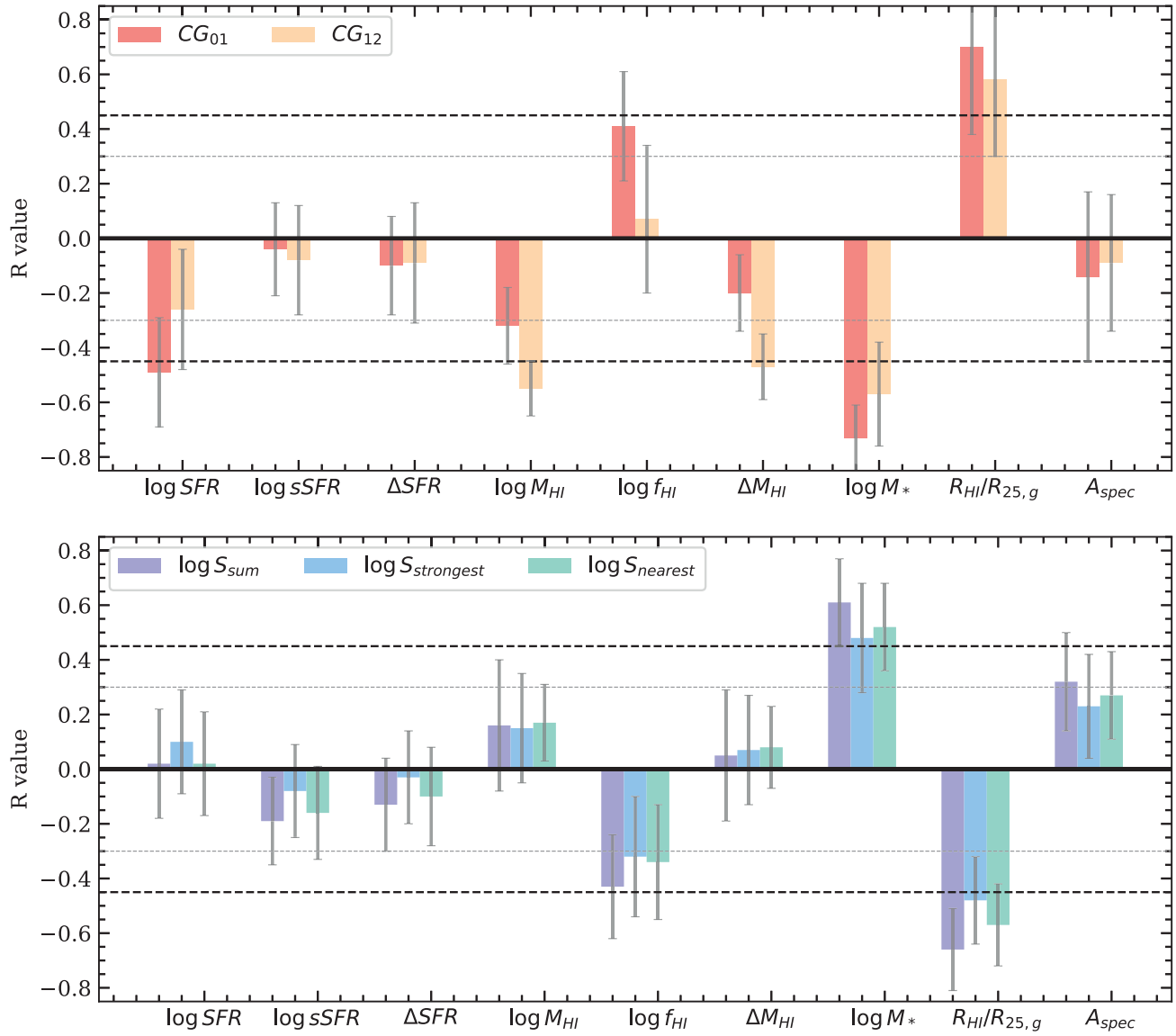


Figure 6. Pearson correlation coefficients for low-mass ($\log M_*/M_\odot < 8.95$) galaxies. Upper: between color gradients (CG_{01} and CG_{12}) and galaxy properties. Lower: between tidal parameters (S_{sum}, $S_{strongest}$, and $S_{nearest}$) and galaxy properties. The dashed black (gray) horizontal line represents $|R| = 0.45$ (0.3), which we regard as the criterion for a significant (considerable) (anti-)correlation. The error in R is derived by bootstrap resampling.

analysis is performed for the low-mass ($\log M_*/M_\odot < 8.95$) and high-mass ($\log M_*/M_\odot > 8.95$) galaxies separately.

4.4.1. Dependence of Color Gradients and Tidal Strengths on Galaxy Properties

The major goal of this section is to identify the parameters that drive variations in the color gradients and in the tidal strengths separately, so that we can control for these major driving parameters when investigating correlations between color gradients and tidal strengths later. The galaxy properties considered here include SFR related measurements such as SFR, sSFR, and ΔSFR, H I related measurements such as $M_{\rm H\,I}$, $f_{\rm H\,I}$, and $\Delta M_{\rm H\,I}$, the stellar mass M_*, the H I to optical disk size ratio $R_{\rm H\,I}/R_{25,g}$ and the H I spectral line asymmetry $A_{\rm spec}$. These parameters have been described in Section 3. In Figure 6 and Table 1 we show the Pearson correlation coefficients (R) for the relation between color gradients and these parameters, and between tidal strengths and these parameters for low-mass galaxies.

As can be seen from Table 1, CG_{01} shows a significant ($|R| > 0.45$, shown in bold) anticorrelation with star formation rate and stellar mass. CG_{12} significantly anticorrelates with H I mass, $\Delta M_{\rm H\,I}$, and stellar mass. All three types of tidal parameters show a significant correlation with stellar mass and a considerable anticorrelation with H I gas fraction. As an example to illustrate the (anti-)correlations, the dependence of CG_{01}, CG_{12}, and $S_{\rm sum}$ on stellar mass is shown in Figure 7.

4.4.2. The Relation between Color Gradients and Tidal Strengths

In Figure 8 and Table 2 we present the Pearson correlation coefficients (R) between color gradients and tidal parameters. For low-mass galaxies, all three types of tidal parameters show a significant anticorrelation with CG_{01} and CG_{12}, with the most significant ones being those with $S_{\rm sum}$. We need to account for

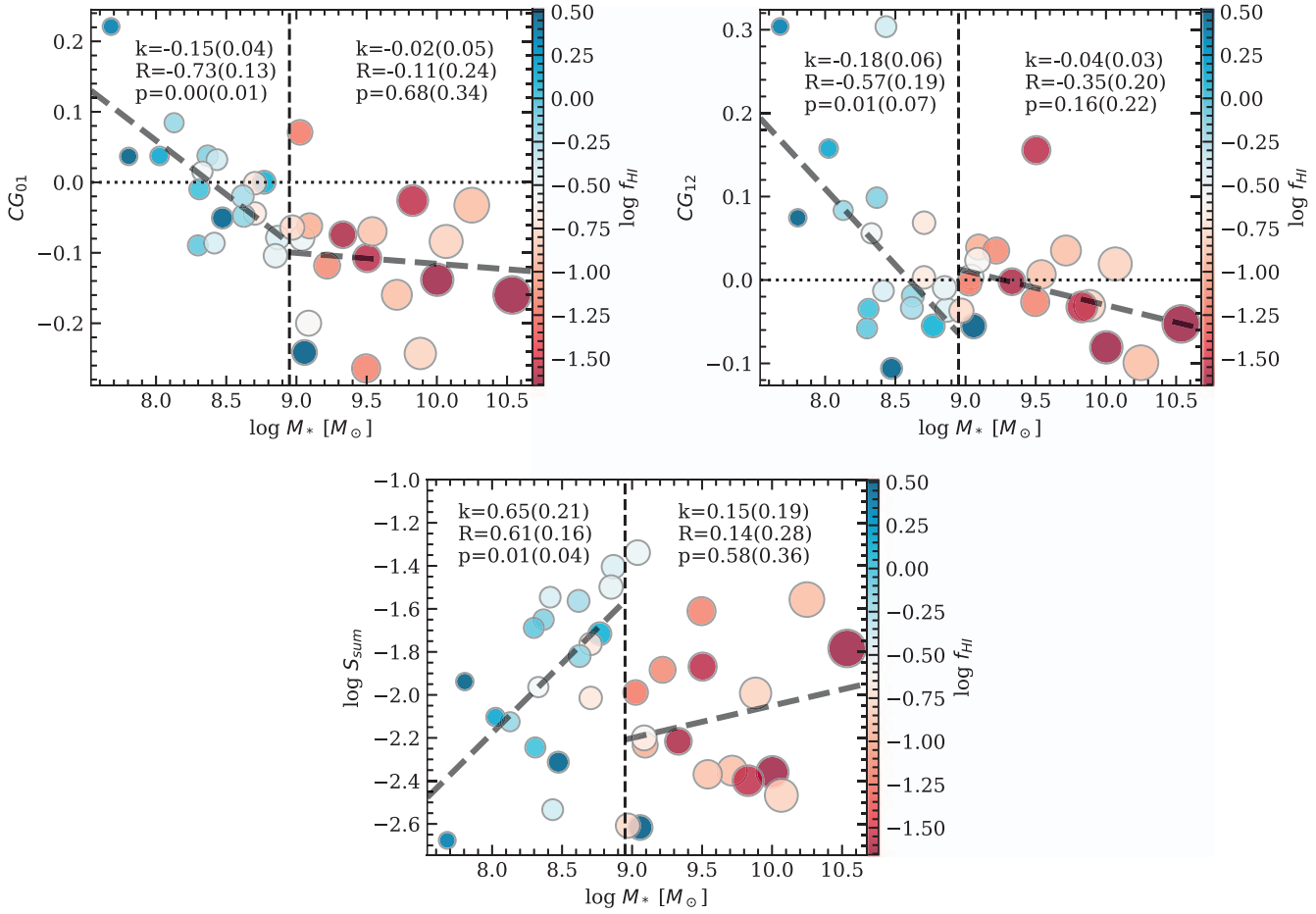


Figure 7. The dependence of color gradients and the summed tidal parameter on stellar mass. The stellar mass division ($M_* = 10^{8.95}\ M_\odot$) of low- and high-mass subsamples is presented by vertical black dashed lines. Upper left: CG_{01}. Upper right: CG_{12}. Lower: S_{sum}. Pearson R and p-values are shown with bootstrap errors in parentheses for both low- ($\log M_*/M_\odot < 8.95$, left) and high-mass ($\log M_*/M_\odot > 8.95$, right) galaxies separately. Gray dashed lines are the result of a robust linear fit, with the slopes (and errors) shown above the R and p-value. All data points are color coded by H I gas fraction (see color bar on the right). The size of data points indicates the stellar mass of the galaxy, in the sense that larger data points are used for more massive galaxies.

Table 1
Pearson Correlation Coefficients (R) and p-values between Color Gradients (CG), Tidal Parameters (S), and Galaxy Properties, for Low-mass ($\log M_*/M_\odot < 8.95$) Galaxies

	CG_{01}	CG_{12}	$\log S_{sum}$	$\log S_{strongest}$	$\log S_{nearest}$
log SFR	**−0.49(0.00)**	−0.26(0.13)	0.02(0.90)	0.10(0.57)	0.02(0.90)
log sSFR	−0.04(0.83)	−0.08(0.64)	−0.19(0.28)	−0.08(0.64)	−0.16(0.37)
ΔSFR	−0.10(0.54)	−0.09(0.60)	−0.13(0.44)	−0.03(0.86)	−0.10(0.54)
$\log M_{H\,I}$	*−0.32(0.19)*	**−0.55(0.02)**	0.16(0.53)	0.15(0.56)	0.17(0.50)
$\log f_{H\,I}$	*0.41(0.10)*	0.07(0.78)	*−0.43(0.08)*	*−0.32(0.20)*	*−0.34(0.17)*
$\Delta M_{H\,I}$	−0.20(0.42)	**−0.47(0.05)**	0.05(0.83)	0.07(0.80)	0.08(0.75)
$\log M_*$	**−0.73(0.00)**	**−0.57(0.01)**	**0.61(0.01)**	**0.48(0.04)**	**0.52(0.03)**
$R_{H\,I}/R_{25,g}$	**0.70(0.00)**	**0.58(0.02)**	**−0.66(0.00)**	**−0.48(0.04)**	**−0.57(0.01)**
A_{spec}	−0.14(0.58)	−0.09(0.71)	*0.32(0.20)*	0.23(0.36)	0.27(0.28)

Note. The p-values are shown in parentheses. The format of the numbers indicates the significance of the correlation: bold for significant ones ($|R| > 0.45$) and italics for those that are considerable ($0.45 > |R| > 0.3$).

the fact that the correlation between color gradient and tidal strength could be due to a third parameter. We thus calculate the partial correlation coefficients between color gradients and tidal parameters with the potential third parameter controlled. The results are shown in Figure 9 and Table 3.

We find that for the low-mass galaxies the anticorrelation between CG_{01} and CG_{12} and tidal parameters (S_{sum}) is still significant when stellar mass is controlled. Similar conclusions are reached when the H I mass or H I gas fraction is controlled. The similarly significant correlations with $S_{nearest}$ and $S_{strongest}$ suggest that tidal effects produced by the nearest and/or the strongest perturber may dominate the effects of tidal interaction on color gradients. Recall that the situation is different when considering the correlations of tidal strengths with the H I

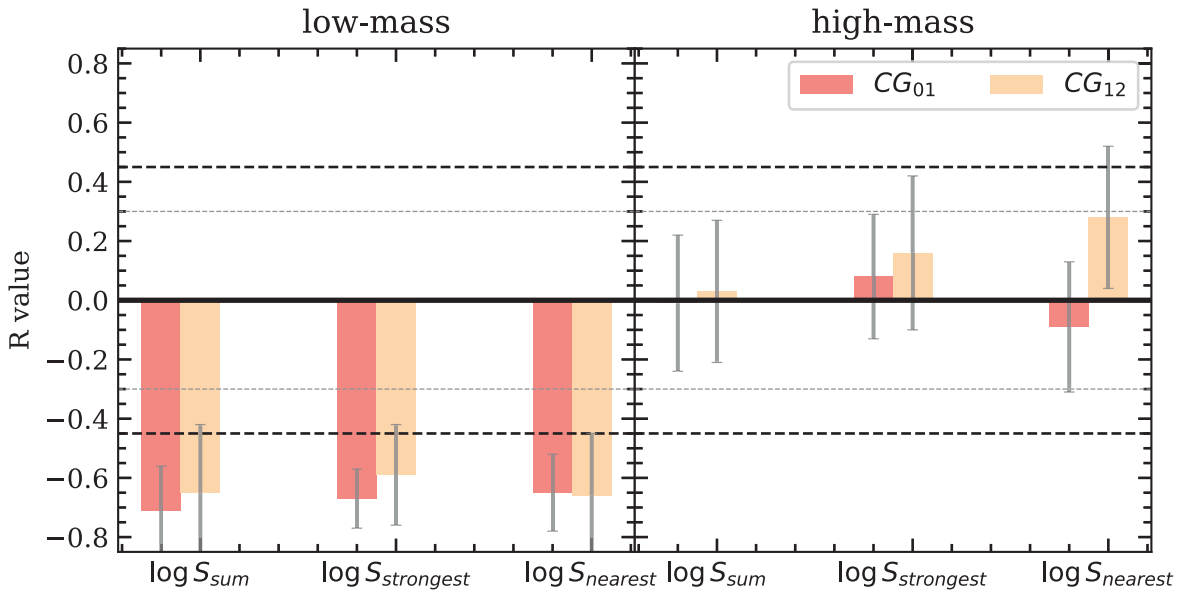


Figure 8. Pearson correlation coefficients between color gradients and tidal parameters. Left: for low-mass ($\log M_*/M_\odot < 8.95$) galaxies. Right: for high-mass ($\log M_*/M_\odot > 8.95$) galaxies. The dashed black (gray) horizontal line represents $|R| = 0.45$ (0.3), which we regard as the criterion for a significant (considerable) (anti-)correlation. The error in R is derived by bootstrap resampling.

Table 2
Pearson Correlation Coefficients (R) and p-values between Color Gradients (CG) and Tidal Parameters (S) for Low-mass ($\log M_*/M_\odot < 8.95$) and High-mass ($\log M_*/M_\odot > 8.95$) Galaxies

	Low-mass			High-mass		
	$\log S_{\rm sum}$	$\log S_{\rm strongest}$	$\log S_{\rm nearest}$	$\log S_{\rm sum}$	$\log S_{\rm strongest}$	$\log S_{\rm nearest}$
CG_{01}	**−0.71(0.00)**	**−0.67(0.00)**	**−0.65(0.00)**	−0.01(0.98)	0.08(0.76)	−0.09(0.71)
CG_{12}	**−0.65(0.00)**	**−0.59(0.01)**	**−0.66(0.00)**	0.03(0.90)	0.16(0.52)	0.28(0.27)

Note. Symbols are the same as in Table 1: p-values are shown in parentheses. The format of the numbers indicates the significance of the correlation: bold for significant ones ($|R| > 0.45$) and italics for those that are considerable ($0.45 > |R| > 0.3$).

spectral asymmetry parameters. We show the relation between $S_{\rm sum}$ and CG_{12}, CG_{01} in Figure 10, with data points color coded by H I gas fraction and their sizes indicating stellar mass.

5. Discussion

5.1. Tidal Effects on the Distribution of H I

The observation of the H I component in the Eridanus supergroup galaxies from WALLABY enables us to probe the most subtle yet direct effects produced by tidal interactions that we might expect. The anticorrelation between $S_{\rm sum}$ and $R_{\rm H\,I}/R_{25,g}$ among low-mass galaxies (Figure 4) suggests the possible existence of stripping effects (e.g., Moore et al. 1999) from tidal interactions. The outer H I disks are preferentially stripped as the gravity is weaker at a larger radius. The stripped H I may be accreted by more massive galaxies, or may disperse in the hot intragroup medium (IGM). Theoretically tidal interactions may cause gas inflow (e.g., Hernquist & Mihos 1995; Mayer et al. 2001), enhance central star formation, and accelerate the consumption of H I, which together may also lead to a shrinkage of the H I disk. However this scenario is unlikely for our low-mass galaxies as the inner color is not bluer, but redder (Figure 11).

Previous studies have shown that image asymmetries in the H I can be caused by galaxy interactions (e.g., Koribalski & López-Sánchez 2009; English et al. 2010; Holwerda et al. 2011). The insignificant correlation between H I spectral line asymmetry and tidal strength we find for Eridanus supergroup galaxies, however, may be due to the incapability of the projected line asymmetry to reflect the three-dimensional true asymmetry caused by perturbations. The weak relation between line asymmetry and environment has been noticed before (Espada et al. 2011; Scott et al. 2014; Reynolds et al. 2020). Although there have been supportive results based on observed and simulated data on the link between enhanced H I line asymmetry, gas loss, and environment density (Watts et al. 2020a; Manuwal et al. 2022), a direct causality by galactic tidal interaction has not been clearly established.

Our findings are thus consistent with the idea that the tidal interaction, as an effective mechanism of external perturbation, can strip H I gas from galaxies and cause the H I disks to shrink. They are consistent with previous findings that ram pressure stripping is unlikely to be the primary driver for galactic H I deficiency in groups with a similar mass to that of Eridanus (Kilborn et al. 2009).

5.2. Color Gradients as a Tracer of Star Formation Distributions

The color of a stellar disk is dependent not only on stellar age, but also on stellar metallicity and dust extinction. Previous studies (de Jong 1996; Bell & de Jong 2000) found that the radial color gradients in disk and spiral galaxies are consistent predominantly with the effects of stellar age

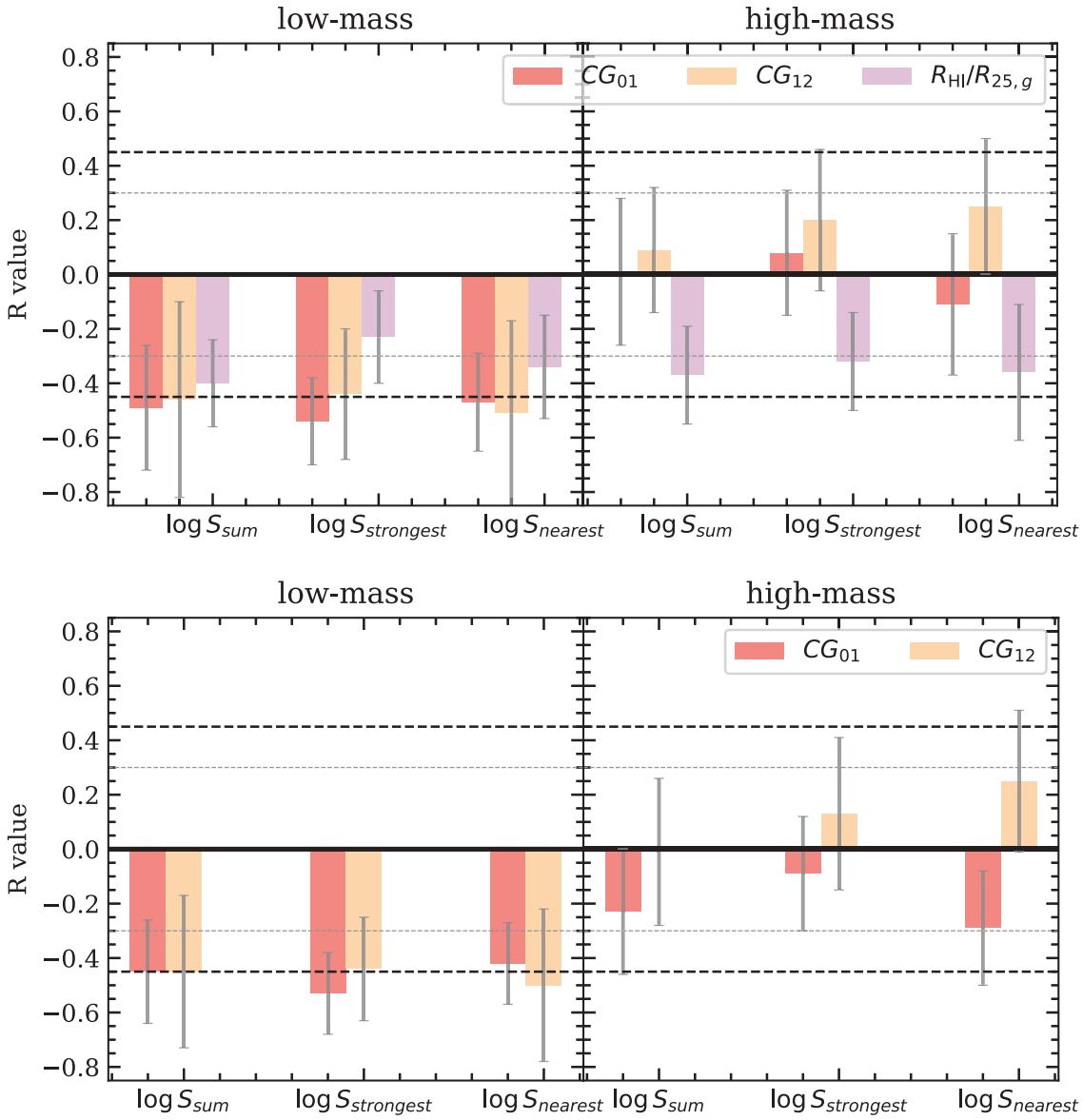


Figure 9. Partial correlation coefficients between color gradients and tidal parameters. Upper: control for stellar mass ($\log M_*$). Lower: control for H I to optical disk sizes ($R_{\rm H\,I}/R_{25,g}$). Left: for low-mass ($\log M_*/M_\odot < 8.95$) galaxies. Right: for high-mass ($\log M_*/M_\odot > 8.95$) galaxies. The black (gray) horizontal line represents for $|R| = 0.45$ (0.3), which we regard as the criterion for a significant (considerable) (anti-)correlation. The error in R is derived by bootstrap resampling.

Table 3

Partial Correlation Coefficients (R) and p-values between Color Gradients (CG), H I to Optical Disk Size Ratios ($R_{\rm H\,I}/R_{25,g}$), and Tidal Parameters (S) for Low-mass ($\log M_*/M_\odot < 8.95$) and High-mass ($\log M_*/M_\odot > 8.95$) Galaxies, with Stellar Masses (M_*, Upper) or H I to Optical Disk Size Ratios ($R_{\rm H\,I}/R_{25,g}$, Lower) Controlled

	Low-mass			High-mass		
	$\log S_{\rm sum}$	$\log S_{\rm strongest}$	$\log S_{\rm nearest}$	$\log S_{\rm sum}$	$\log S_{\rm strongest}$	$\log S_{\rm nearest}$
CG_{01}	**−0.49(0.05)**	**−0.54(0.03)**	**−0.47(0.06)**	0.01(0.98)	0.08(0.75)	−0.11(0.68)
CG_{12}	**−0.46(0.06)**	*−0.44(0.08)*	**−0.51(0.04)**	0.09(0.74)	0.20(0.44)	0.25(0.33)
$R_{\rm H\,I}/R_{25,g}$	*−0.40(0.11)*	−0.23(0.37)	*−0.34(0.18)*	*−0.37(0.14)*	*−0.32(0.21)*	*−0.36(0.16)*
	$\log S_{\rm sum}$	$\log S_{\rm strongest}$	$\log S_{\rm nearest}$	$\log S_{\rm sum}$	$\log S_{\rm strongest}$	$\log S_{\rm nearest}$
CG_{01}	**−0.45(0.07)**	**−0.53(0.03)**	*−0.42(0.09)*	−0.23(0.37)	−0.09(0.72)	−0.29(0.25)
CG_{12}	**−0.45(0.07)**	*−0.44(0.08)*	**−0.50(0.04)**	−0.01(0.96)	0.13(0.61)	0.25(0.33)

Note. Symbols are as in Table 1: p-values are shown in parentheses. The format of the numbers indicates the significance of the correlation: bold for significant ones ($|R| > 0.45$) and italics for those that are considerable ($0.45 > |R| > 0.3$).

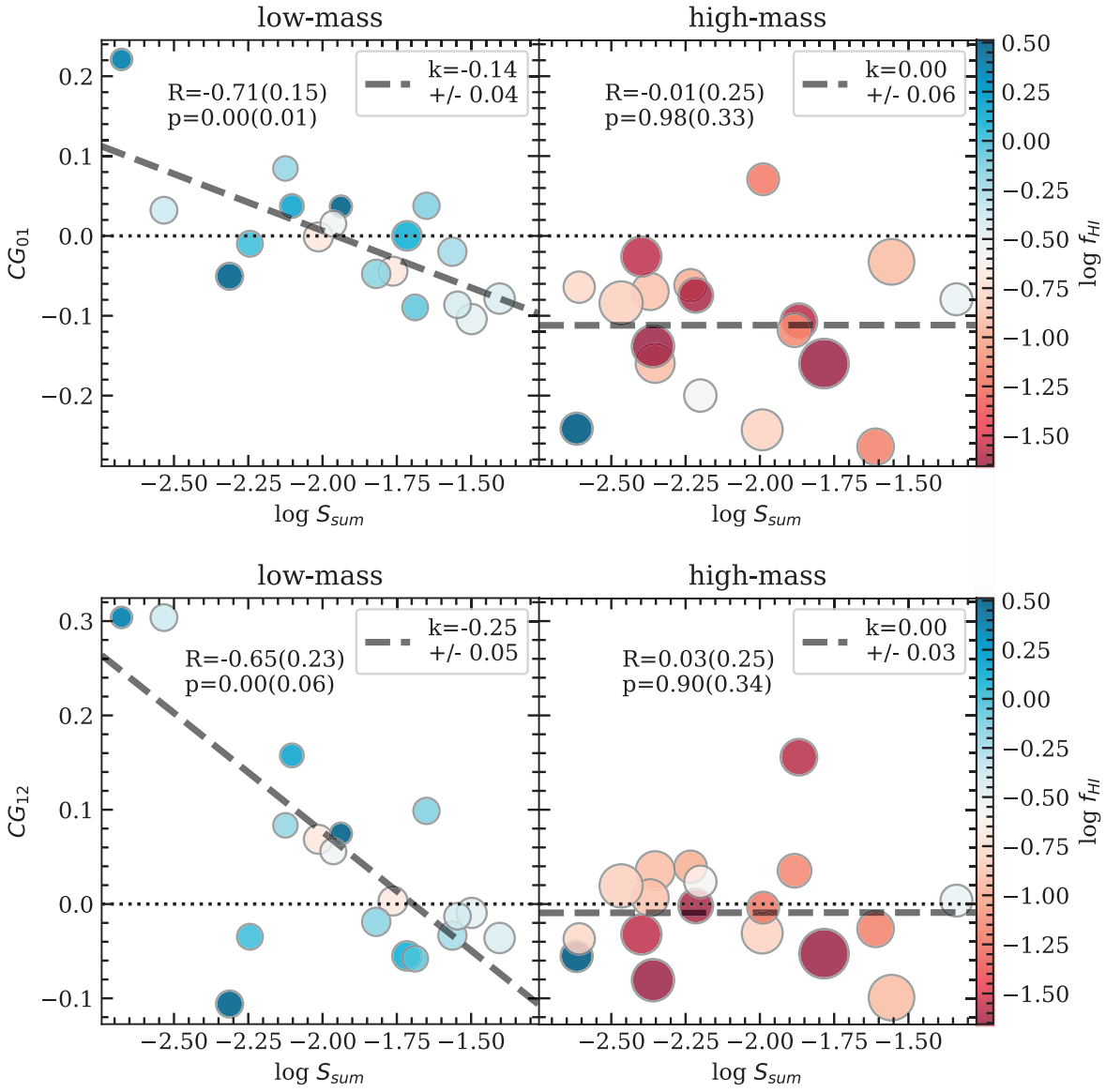


Figure 10. The correlation between color gradients and the summed tidal parameters. The dotted horizontal lines represent $CG_{01} = 0$ and $CG_{12} = 0$, respectively. Left: for low-mass ($\log M_*/M_\odot < 8.95$) galaxies. Right: for high-mass ($\log M_*/M_\odot > 8.95$) galaxies. The other symbols and text are the same as in Figure 3: Pearson R and p-values are shown with bootstrap errors in parentheses. Gray dashed lines are the result of a robust linear fit, with the slopes (and errors) shown in the corner. All data points are color coded by H I gas fraction (see color bar on the right). The size of data points indicates the stellar mass of the galaxy, in the sense that larger data points are used for more massive galaxies.

gradients. Gadotti & dos Anjos (2001) also claimed that dust is unlikely to play a fundamental role in global color gradients in late-type spiral galaxies. It is thus reasonable to assume that the color gradients represent stellar age gradients and the disk assembly history of our galaxies. This method was used by Wang et al. (2011) to study the connection between H I and disk assembly, and was also used by many studies to investigate the connection between environmental effects and radial star formation enhancement and quenching (e.g., Weinmann et al. 2006; Pan et al. 2018, 2019; Patton et al. 2020).

The dependence of color gradients on stellar mass has been extensively studied in the literature. It was found that more massive galaxies tend to show negative or flat color gradients while low-mass galaxies tend to show positive color gradients (e.g., Tortora et al. 2010; Gonzalez-Perez et al. 2011; Cibinel et al. 2013). Figure 5 confirms this transition with stellar mass. It was also found that relatively less massive galaxies tend to show positive color gradients when they are in the green valley and/or of early-type (Pan et al. 2015, 2016; Belfiore et al. 2018; see also Cibinel et al. 2013). However, our sample of galaxies (both low- and high-mass subsets) are biased against green-valley galaxies and early-type galaxies (see For et al. 2021), thus our results cannot be directly compared to these trends.

In the following, we discuss the influence of tidal interactions on the color gradients for the low- and high-mass galaxies separately.

5.2.1. Tidal Effects on Color Distribution in Low-mass Galaxies

Based on a sample of 34 Local Volume low-mass galaxies (all with $M_* < 10^9\ M_\odot$ except for one galaxy with $M_* = 1.2 \times 10^9\ M_\odot$), Zhang et al. (2012) found that, contrary to the high-mass galaxies, these low-mass galaxies typically show positive color gradients (i.e., blue cores). They considered in situ star formation,

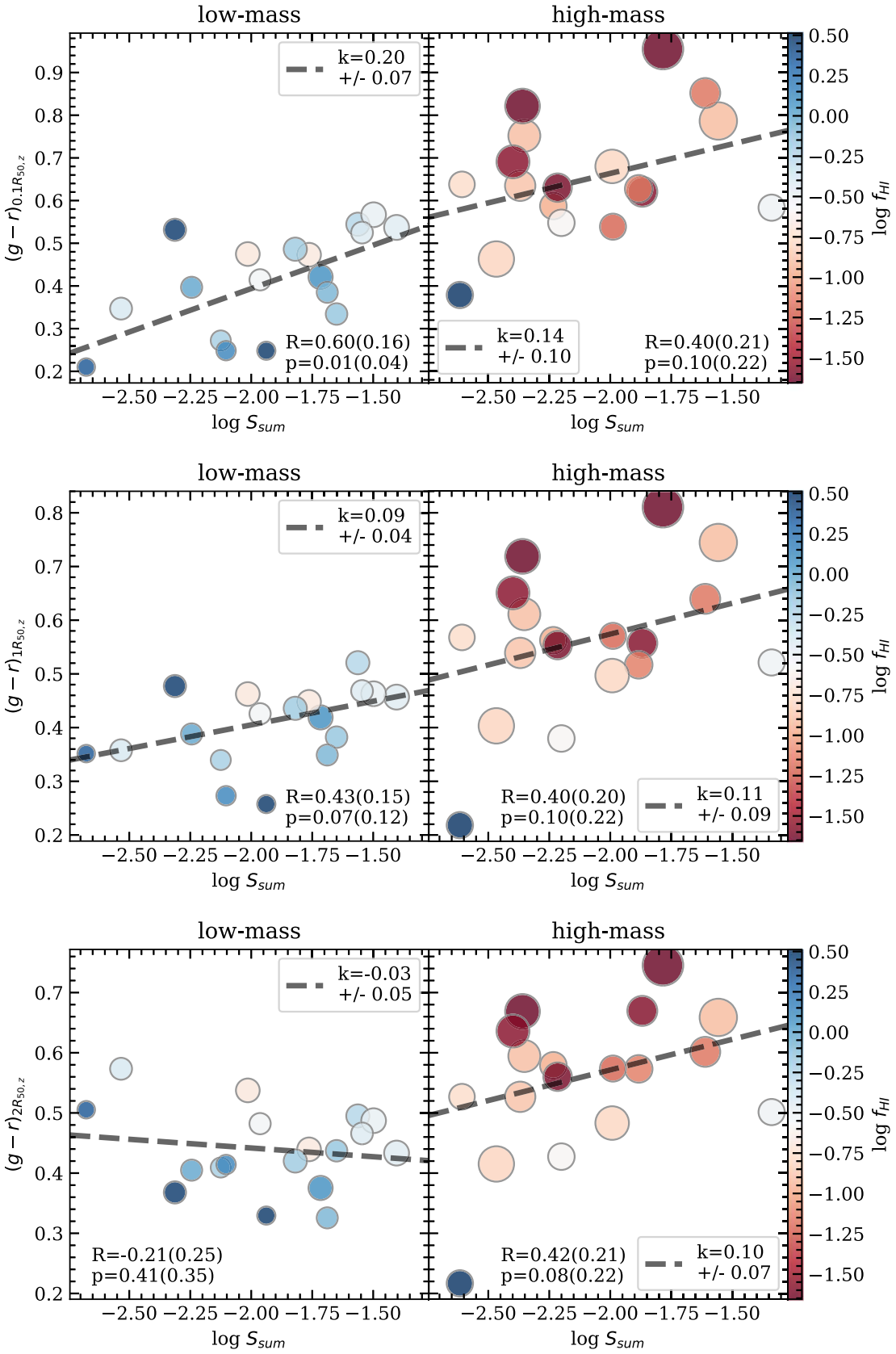


Figure 11. The correlation between $g-r$ color at different radius and the summed tidal parameters. Top: at $R\sim 0.1R_{50,z}$. Middle: at $R\sim R_{50,z}$. Bottom: at $R\sim 2R_{50,z}$. The symbols and text are the same as in Figure 3: Pearson R and p-values are shown with bootstrap errors in parentheses. Gray dashed lines are the result of a robust linear fit, with the slopes (and errors) shown in the corner. All data points are color coded by H I gas fraction (see color bar on the right). The size of data points indicates the stellar mass of the galaxy, in the sense that larger data points are used for more massive galaxies.

secular redistribution, external influence (e.g., ram pressure stripping and tidal interaction), regulation of star formation through stellar feedback, and gas pressure supported dynamics as potential causes, but, possibly due to the limited sample size and selection effects, they did not find conclusive observational evidence that showed why blue cores were dominant. Later models were proposed to explain the radial distribution of stellar age in these dwarf irregular galaxies as a consequence of fountain driven accretion (Elmegreen et al. 2014), and stellar feedback driven, age-dependent stellar migration (e.g., El-Badry et al. 2016). More recently, the local SFR was found to follow the volumetric star formation law of more massive galaxies, where the volumetric density was derived assuming a hydrostatic quasi-equilibrium between the gravitational potential and the kinetic energy of the gas (Bacchini et al. 2020). As the color is correlated with sSFR, the radial distribution of the color may be a natural consequence of the balanced radial distribution of the SFR, the gas mass, and the stellar mass. Common features of these models are that the relevant low-mass galaxies are relatively unperturbed by the environment, and their star formation is fueled in a relatively quasi-equilibrium state.

In our study, the overall color gradients of the low-mass galaxies are much more positive than those of the high-mass galaxies, consistent with the findings of Zhang et al. (2012). Moreover, we find a clear trend of more negative color gradients within $2R_{50,z}$ under stronger external tidal interaction, highlighting the important role of external tidal effects in modifying the star formation distribution in the low-mass galaxies.

There are two observational possibilities to explain why the low-mass galaxies have more negative CG_{01} and CG_{12} when S_{sum} increases: either the inner color becomes redder, or the outer color becomes bluer. We distinguish these two possibilities by investigating the dependence of the $g-r$ colors close to $0.1R_{50,z}$, $R_{50,z}$, and $2R_{50,z}$ on the S_{sum} parameter (Figure 11). We find that the $g-r$ color at the center, i.e., $(g-r)_{0.1R_{50,z}}$, shows the most significant correlation with S_{sum} and the correlation for $(g-r)_{1R_{50,z}}$ is weaker but still noticeable, while $(g-r)_{2R_{50,z}}$ only shows a tentative anticorrelation with S_{sum}. Therefore, the drop of the color gradients in these low-mass galaxies is mainly because the inner regions are redder and not because the outer regions are bluer. The star formation is not strongly enhanced in the outer disk, although simulations predict and observations partially support that this could happen as a result of enhanced local gas densities and instabilities (e.g., Pan et al. 2019; Moreno et al. 2021). Instead, the star formation, which could have been concentrated in the inner disks and show a positive color gradient if these low-mass galaxies were in an isolated environment, is likely suppressed by the tidal perturbations.

One worry however may arise that the central colors can be redder because of a higher level of dust attenuation, caused by a large amount of centrally concentrated dust, transported there with gas inflows driven by tidal interactions (e.g., Hernquist & Mihos 1995; Mayer et al. 2001). We thus conduct the following test. We take SFR_{W4} as the dust attenuated part of the SFR (see Section 2), and use SFR_{W4}/SFR to infer A_{FUV} or A_{NUV}, depending on which of the two ultraviolet bands is used in estimating SFR. When W4 fluxes are not detected, we use the fifth percentile of the W4 flux distribution in our sample as the upper limit. We use the extinction curve of Wyder et al. (2007) for the ultraviolet bands, where $A_{FUV}=8.24E(B-V)$ and $A_{NUV}=8.2E(B-V)$, and the extinction curve of Calzetti et al. (2000) for the optical bands where $A_g-A_r=1.16E(B-V)$. Hence, $A_g-A_r=0.14A_{FUV}=0.14A_{NUV}$. Limited by the large point-spread function of GALEX and WISE images, we are unable to directly trace the attenuation near $0.1R_{50}$, which is typically below $5''$ in the low-mass subsample. Although A_g-A_r is a measure for the global level of attenuation, it should be biased toward the condition in the galactic center if the centrally concentrated dust (and hence gas and starburst) dominates the reddening of the central color. In Figure 12, we show the relation between A_g-A_r and S_{sum} for the low-mass subsample. There is no significant correlation. More importantly, there should have been a trend for A_g-A_r to increase with S_{sum}, if the reddening of the central $g-r$ color had been caused by centrally concentrated dust, but there is no evidence for such a trend. We thus conclude that the reddening of the central color with S_{sum} should be more likely associated with an old stellar population than with a high dust attenuation.

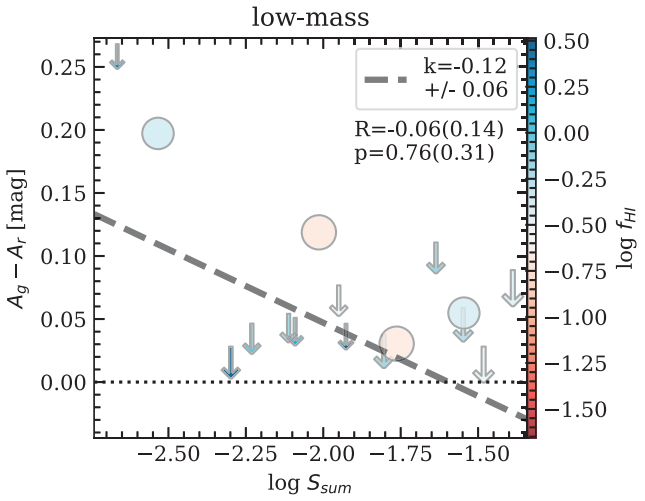


Figure 12. The correlation between color excess and the summed tidal parameters for low-mass galaxies. The dotted horizontal lines represent $A_g-A_r=0$. The downward arrows are upper limits of the color excess. The other symbols and text are the same as in Figure 3: Pearson R and p-value are shown with bootstrap errors in parentheses. The gray dashed line is the result of a linear fit (upper limits taken into account), with the slope (and error) shown in the corner. All data points are color coded by H I gas fraction (see color bar on the right). The size of data points indicates the stellar mass of the galaxy, in the sense that larger data points are used for more massive galaxies.

In addition to the reddening of inner disks, we find on average a decrease in relative size ($R_{H\,I}/R_{25,g}$) with increasing S_{sum}. On average, H I disk size becomes smaller than that of the optical disk (Figure 4) and CG_{01} becomes negative (upper panel of Figure 10) simultaneously at the characteristic $S_{sum}\sim 0.01$. The suppression of the SFR is thus likely linked to the removal of the gas reservoir, probably as well as the decreased star-forming efficiency, when the increase in the velocity dispersion stabilizes the gas against gravitational collapse and/or radial inflow (e.g., Bigiel et al. 2008; Leroy et al. 2008). It is interesting to point out that the characteristic S_{sum} of $\sim$0.01 is much lower than the critical value of 0.07 for stellar disks to be strongly perturbed as predicted in previous stellar-only N-body simulations (Oh et al. 2008). It highlights the H I gas and star formation as more sensitive tracers to tidal perturbation than the morphology and mass of the stellar disks.

5.2.2. Tidal Effects on Color Distribution in High-mass Galaxies

High-mass galaxies typically show negative color gradients (i.e., red cores), which is consistent with a scenario where the galactic disks form inside-out, driven by the cosmic gas accretion (Mo et al. 1998). Such a scenario is confirmed by the observed dependence of color gradients on H I gas fractions at a given stellar mass in high-mass galaxies (Wang et al. 2011). Our results confirm the dependence of color gradients on H I mass or H I excess with the high-mass subset, and find that the trend holds in the low-mass galaxies, supporting the important role of H I abundance in shaping the stellar disks. Large-scale cosmic gas accretion onto low-mass satellite galaxies was hinted at before by the observational conformity phenomenon (Kauffmann et al. 2013; Kauffmann 2015; Wang et al. 2015).

On top of the general behaviors of galaxies, tidal interactions have been found to be an important factor significantly affecting the color gradients of massive galaxies. High-mass galaxies with close companions were found to have on average $\sim$0.2 mag bluer bulges and $\sim$0.1 mag redder disks than the isolated control galaxies (Ellison et al. 2010), consistent with a scenario where tidal interactions induce gas inflows, either through bar instability (e.g., Barnes & Hernquist 1996; Mayer et al. 2001) or through gravitational torques (e.g., Hernquist & Mihos 1995) that boost the gas density (e.g., Hibbard & van Gorkom 1996; Rupke et al. 2010; Dekel & Burkert 2014; Zolotov et al. 2015; Chown et al. 2019) and thus significantly elevate the SFR in the center (e.g., Barton Gillespie et al. 2003; Kewley et al. 2006; Ellison et al. 2008). Fernández Lorenzo et al. (2014) also found that, in a sample of highly isolated massive galaxies, most bulges are as red as E galaxies, but the subsample of bluer bulges is more likely to be located in galaxies with a higher likelihood of (minor) tidal perturbations. But the previous studies also found that the link between elevated central SFR and a close companion disappears when the galaxy pairs are in high-density environments ($\log\Sigma > 0.15$, where $\log\Sigma \equiv \frac{1}{2}\log\left(\frac{4}{\pi d_4^2}\right) + \frac{1}{2}\log\left(\frac{4}{\pi d_5^2}\right)$ and d_4 and d_5 are the projected distances to the fourth and fifth nearest neighbors within 1000 km s^{-1}) or have large separations ($r_p > 30h_{70}^{-1}$ kpc) at intermediate densities ($-0.55 < \log\Sigma < 0.15$), which was speculatively attributed to lower gas fractions in such environments (Alonso et al. 2004; Ellison et al. 2010). We adopt the same magnitude cut as that of Ellison et al. (2010) and derive an averaged $\log\Sigma$ of -0.14 and $D_{\rm nearest}$ of $\gtrsim$500 kpc for the Eridanus supergroup region. Thus the small dependence of the color gradients on the S parameters for our high-mass subset is consistent with previous findings.

Since the S parameter of the high-mass galaxies has a similar range to that of low-mass galaxies, the weak trend in their color gradients is unlikely due to their stronger gravity. We note that the S parameters adopted in this paper principally probe the tidal strength at the edge of the optical disks, and $R_{\rm H\,I}$ values are smaller than R_{25} in most of the high-mass galaxies (see Figure 4). It is thus likely that only a small fraction of these truncated H I disks suffer significantly from the effect of tidal interactions. Since the H I is an important intermediate step in fueling star formation (Wang et al. 2020), little influence on the H I mass may have led to a low gas inflow rate, and barely any enhancement in the central SFR.

That said, we do observe a correlation between the colors throughout the disks (at $0.1R_{50,z}$, $1R_{50,z}$, and $2R_{50,z}$) and tidal strengths despite the relatively large scatter (see the right column of Figure 11). It implies that tidal stripping does contribute to accelerating the SFR quenching of these massive galaxies, but the averaged pattern is not inside-out as it would be in the low-mass galaxies of this study, or in general high-mass galaxies (Ellison et al. 2018b). Unlike in the low-mass galaxies, the general H I rich high-mass galaxies tend to have a higher specific SFR and bluer colors in the outer disks than in the inner disks when they are unperturbed (Wang et al. 2011), which might have resulted in the outer disk colors being more sensitive to the stripping of H I than would be the case in low-mass galaxies.

It is also interesting to point out that, for both low- and high-mass galaxies in the H I sample, the correlation between tidal strength and color gradient seems stronger than that between tidal strength and H I content (i.e., $f_{\rm H\,I}$ and $M_{\rm H\,I}$). For et al. (2021) also found that the global SFR of the H I sample is not strongly suppressed in galaxies of Eridanus supergroup. Such results suggest that the tidal perturbation as quantified in this paper is likely to more efficiently affect the radial distribution of star formation (and likely also H I) instead of the total amount. Thus we see stronger correlations between tidal strengths and color gradients than between tidal strengths and the amount of H I content. It is also hinted that tidal interactions that are not able to strip gas from the galaxy may have significant effects on the distribution of gas and star formation.

5.3. Other Environmental Effects

We consider two additional environmental effects that may play a role in the galaxies of this paper. First, we consider the tidal force from the group halo, the mass of which is dominated by the dark matter halo (e.g., Valluri 1993; Henriksen & Byrd 1996; Fujita 1998). Unlike galaxy–galaxy tidal interactions, interaction with the group halo is more likely to drive gas inflows than to strip the gas. The strength of the effect can be quantified as $P_{\rm gc} = (M_{\rm cluster}/M_{\rm gal})(R/r_{\rm gal})^{-3}$ (Byrd & Valtonen 1990). A threshold value above which significant disk instabilities and thus gas inflows can be triggered is predicted to range from 0.006 to 0.1 depending on the ratio of dark matter halo mass over the disk mass (Byrd & Valtonen 1990). We estimate that the sum of tidal forces from the groups (Eridanus, the NGC 1407 group, and the NGC 1332 group) enforced on each galaxy ranges from 3×10^{-6} to 0.1, with five (four) high-mass (low-mass) galaxies having a tidal force from any of the groups larger than 0.006. Thus, tidal interaction with the group halo is unlikely to be the dominating effect among the whole sample, but may affect a few galaxies close to group centers. However, we do not observe peculiar color distributions in those galaxies with $P_{\rm gc} > 0.006$, possibly because the interaction with the group halo is not strong enough to counteract the stripping effect from other galaxies, or because projection effects have led to large uncertainties in the estimate of $P_{\rm gc}$ due to inaccurate estimate of the group-centric distances.

A second effect we consider is ram pressure stripping due to the hot IGM. We follow the method of Wang et al. (2020, 2021) to compare the ram pressure level with disk restoring forces on the H I gas. We estimate the IGM density at the location of each galaxy by interpolating (extrapolating for galaxies in the NGC 1332 group and the Eridanus group) the gas density profile of the NGC 1407 group, because extended X-ray emission is only detected in the core region of the NGC 1407 group. Most of the galaxies in the H I sample have projected distances to NGC 1407 in the range of $1.25R_{\rm virial}$ to

$3.5R_{\rm virial}$. It is thus natural to expect a weak level of ram pressure stripping effects on galaxies in the Eridanus supergroup. And, indeed, there are only three, i.e., NGC 1390 (ID 21), ESO 548-65 (ID 23), and NGC 1359 (ID 69), out of 36 galaxies identified to be candidates for ram pressure stripping, which experience higher ram pressure than the gravitational restoring forces at $R_{\rm H\,I}$. Among these three candidates, NGC 1359 is a merging pair, and thus the ram pressure stripping could be assisted by tidal effects when the H I is tidally shifted to regions of low restoring forces. Thus, ram pressure stripping should not play an important role in setting the statistical behavior of this sample. But we point out that the density of the IGM has been assumed to be distributed smoothly following the standard beta model as in Wang et al. (2020, 2021), while cold fronts due to shocks are found to be prevalent in merging clusters (Markevitch & Vikhlinin 2007). A more detailed analysis awaits modeling based on deeper X-ray images, possibly when eROSITA (Merloni et al. 2012) results become available in the near future.

5.4. Caveats and Future Perspective

We emphasize that the systematic uncertainty due to projection effects (both in distance and velocity) and the crude estimation of the duration of the tidal encounter inevitably limit the use of the tidal parameter. Thus it should be considered in a relative sense and is only valid for a statistically meaningful sample. As mentioned in Sections 3.2 and 4.2, the tidal strength parameter has uncertainties contributed by the orbital history of the galaxies, and is particularly not suitable for describing gravitational effects at the coalescence stage of mergers. These types of systems are few in our H I sample, but an alternative way of quantifying the physical effects in the coalescence stage should be considered in the future.

As the Eridanus supergroup is in a distinct stage of cluster or supergroup assembly, it is likely that tidal interactions are enhanced. It will be meaningful to apply the technique used in this paper to more general groups in the future, when the WALLABY survey has covered a much larger sky region. Finally, comparing the newly observed results with hydrodynamic simulations using a consistent parameterization will be useful to understand the systematic uncertainties, and derive further insight into complex physical processes that are difficult to address with observations alone, in particular in helping to disentangle the combined effects of tidal interaction and ram pressure stripping, and the cosmological background of group assembly, which sets the initial conditions of galaxies upon infall.

It is worth mentioning that the truncated H I disks of high-mass galaxies indicate pre-processing by the environment outside the current field of view of the Eridanus supergroup. Alternatively, evolution of high-mass galaxies can be more strongly driven by internal structures or masses than by the environment (e.g., Peng et al. 2010). To clarify the evolutionary track of high-mass galaxies, we will need to trace them back to a larger group-centric radius, or consider smaller galaxy groups. In future work we will address this question for other clusters and groups, partly by exploiting additional WALLABY data.

6. Summary and Conclusion

To summarize, we conducted photometric measurements in g, r, and z bands for 36 WALLABY H I detected galaxies in the Eridanus supergroup, and derived color gradients and tidal parameters based on an optical sample of Eridanus supergroup member galaxies. We confirm that the tidal parameters are capable of reflecting the tidal disturbance experienced by, at least, the H I disks, in the sense that the shrinkage of H I disks are connected to large tidal parameters. We do not find clear evidence for the asymmetry of the integral H I spectra to increase with the tidal parameter, possibly because the spatial information is lost in the integral H I spectra. It is worth noting that the tidal perturbation in the Eridanus supergroup is contributed by a significant number of neighboring galaxies, which emphasizes the importance of adopting a complete sample to study tidal interaction in galaxy groups.

We show that the color profiles of galaxies in the Eridanus supergroup are strongly dependent on stellar mass. The color profiles show a transition from a generally positive gradient (redder toward large radii, an outside-in scheme) at the low-mass end ($\log M_*/M_\odot \lesssim 8.5$), to a tentative "U"-shape at intermediate mass ($8.5 \lesssim \log M_*/M_\odot \lesssim 9.5$), and finally to a negative gradient (bluer toward large radii, an inside-out scheme) at the high-mass end ($\log M_*/M_\odot \gtrsim 9.5$), which is consistent with previous findings.

We find that tidal interactions play an important role in determining the color gradients within $2R_{50,z}$ of low-mass galaxies in groups. More negative color gradients (i.e., redder cores and/or bluer outer regions) are clearly related to stronger tidal strengths. Further investigation reveals that the anticorrelation between color gradients and tidal strengths largely originates from the reddening of the central regions rather than bluer outer regions. High-mass galaxies, by contrast, do not show a clear correlation between color gradients and tidal strengths. The colors at all three radii ($0.1R_{50,z}$, $1R_{50,z}$, and $2R_{50,z}$) do correlate with tidal strengths, although with large scatter. These results suggest that the quenching in high-mass galaxies can be assisted by tidal perturbation, but not in a normally expected inside-out way.

Combining the results above, we conclude that tidal interaction in the Eridanus supergroup serves as a major mechanism for star formation quenching in low-mass galaxies. It works by stripping the H I gas from the extended H I disk; as the reservoir of H I shrinks, the inner disk where star formation is concentrated is less fueled than it would be in an unperturbed state. By contrast, the smaller H I reservoir leaves less space for the same mechanism to work in high-mass galaxies of the Eridanus supergroup. Their SFRs throughout the disks are suppressed, possibly due to the halt of their normal inside-out formation as a result of the shrinking H I reservoir at the outskirts of the disk.

We thank the referee for the very constructive, helpful comments.

J.W. acknowledges support from the National Science Foundation of China (12073002 and 11721303), and the science research grants from the China Manned Space Project with No. CMS-CSST-2021-B02. Parts of this research were supported by High-performance Computing Platform of Peking University.

F.B. acknowledges funding from the European Research Council (ERC) under the European Union's Horizon 2020 research and innovation program (grant agreement No. 726384/Empire).

A.B. acknowledges support from the Centre National d'Etudes Spatiales (CNES), France.

Parts of this research were supported by the Australian Research Council Centre of Excellence for All Sky Astrophysics in 3 Dimensions (ASTRO 3D), through project number CE170100013.

This project has received funding from the European Research Council (ERC) under the European Union's Horizon 2020 research and innovation program (grant agreement No. 679627; project name FORNAX).

The Australian SKA Pathfinder is part of the Australia Telescope National Facility which is managed by CSIRO. Operation of ASKAP is funded by the Australian Government with support from the National Collaborative Research Infrastructure Strategy. ASKAP uses the resources of the Pawsey Supercomputing Centre. Establishment of ASKAP, the Murchison Radio-astronomy Observatory and the Pawsey Supercomputing Centre are initiatives of the Australian Government, with support from the Government of Western Australia and the Science and Industry Endowment Fund. We acknowledge the Wajarri Yamatji people as the traditional owners of the Observatory site.

This research has made use of the NASA/IPAC Extragalactic Database, which is funded by the National Aeronautics and Space Administration and operated by the California Institute of Technology.

The Legacy Surveys consist of three individual and complementary projects: the Dark Energy Camera Legacy Survey (DECaLS; Proposal ID #2014B-0404; PIs: David Schlegel and Arjun Dey), the Beijing-Arizona Sky Survey (BASS; NOAO Prop. ID #2015A-0801; PIs: Zhou Xu and Xiaohui Fan), and the Mayall z-band Legacy Survey (MzLS; Prop. ID #2016A-0453; PI: Arjun Dey). DECaLS, BASS, and MzLS together include data obtained, respectively, at the Blanco telescope, Cerro Tololo Inter-American Observatory, NSF's NOIRLab; the Bok telescope, Steward Observatory, University of Arizona; and the Mayall telescope, Kitt Peak National Observatory, NOIRLab. The Legacy Surveys project is honored to be permitted to conduct astronomical research on Iolkam Du'ag (Kitt Peak), a mountain with particular significance to the Tohono O'odham Nation.

NOIRLab is operated by the Association of Universities for Research in Astronomy (AURA) under a cooperative agreement with the National Science Foundation.

This project used data obtained with the Dark Energy Camera (DECam), which was constructed by the Dark Energy Survey (DES) collaboration. Funding for the DES Projects has been provided by the U.S. Department of Energy, the U.S. National Science Foundation, the Ministry of Science and Education of Spain, the Science and Technology Facilities Council of the United Kingdom, the Higher Education Funding Council for England, the National Center for Supercomputing Applications at the University of Illinois at Urbana−Champaign, the Kavli Institute of Cosmological Physics at the University of Chicago, Center for Cosmology and Astro-Particle Physics at the Ohio State University, the Mitchell Institute for Fundamental Physics and Astronomy at Texas A&M University, Financiadora de Estudos e Projetos, Fundacao Carlos Chagas Filho de Amparo, Financiadora de Estudos e Projetos, Fundacao Carlos Chagas Filho de Amparo a Pesquisa do Estado do Rio de Janeiro, Conselho Nacional de Desenvolvimento Cientifico e Tecnologico and the Ministerio da Ciencia, Tecnologia e Inovacao, the Deutsche Forschungsgemeinschaft and the Collaborating Institutions in the Dark Energy Survey. The Collaborating Institutions are Argonne National Laboratory, the University of California at Santa Cruz, the University of Cambridge, Centro de Investigaciones Energeticas, Medioambientales y Tecnologicas−Madrid, the University of Chicago, University College London, the DES −Brazil Consortium, the University of Edinburgh, the Eidgenossische Technische Hochschule (ETH) Zurich, Fermi National Accelerator Laboratory, the University of Illinois at Urbana−Champaign, the Institut de Ciencies de l'Espai (IEEC/CSIC), the Institut de Fisica d'Altes Energies, Lawrence Berkeley National Laboratory, the Ludwig Maximilians Universitat Munchen and the associated Excellence Cluster Universe, the University of Michigan, NSF's NOIRLab, the University of Nottingham, the Ohio State University, the University of Pennsylvania, the University of Portsmouth, SLAC National Accelerator Laboratory, Stanford University, the University of Sussex, and Texas A&M University.

BASS is a key project of the Telescope Access Program (TAP), which has been funded by the National Astronomical Observatories of China, the Chinese Academy of Sciences (the Strategic Priority Research Program "The Emergence of Cosmological Structures" grant No. XDB09000000), and the Special Fund for Astronomy from the Ministry of Finance. The BASS is also supported by the External Cooperation Program of Chinese Academy of Sciences (grant No.# 114A11KYSB20160057), and Chinese National Natural Science Foundation (grant No. 11433005).

The Legacy Survey team makes use of data products from the Near-Earth Object Wide-field Infrared Survey Explorer (NEOWISE), which is a project of the Jet Propulsion Laboratory/California Institute of Technology. NEOWISE is funded by the National Aeronautics and Space Administration.

The Legacy Surveys imaging of the DESI footprint is supported by the Director, Office of Science, Office of High Energy Physics of the U.S. Department of Energy under Contract No. DE-AC02-05CH1123, by the National Energy Research Scientific Computing Center, a DOE Office of Science User Facility under the same contract; and by the U.S. National Science Foundation, Division of Astronomical Sciences under Contract No. AST-0950945 to NOAO.

S.H.O. acknowledges support from the National Research Foundation of Korea (NRF) grant funded by the Korea government (Ministry of Science and ICT: MSIT) (No. NRF-2020R1A2C1008706).

Appendix A
Measurements of Disk Sizes

A.1. Disk Scale Length as the Measure of Optical Disk Sizes

The majority of the galaxies in the H I sample are faint dwarf galaxies. Thus it may be a concern that a surface brightness cut at 25 mag arcsec^{-2} does not enclose the bulk of the galaxy light, so that $R_{25,g}$ is not an ideal quantification of the galaxy size in this study. One of the size estimations that is less affected by the faintness is the disk scale length (assuming exponential disks). We derive the disk scale length (R_d) by fitting the outer disk surface brightness profile in g band and use $4R_d$ as the estimate of disk size (enclosing ∼90% of light,

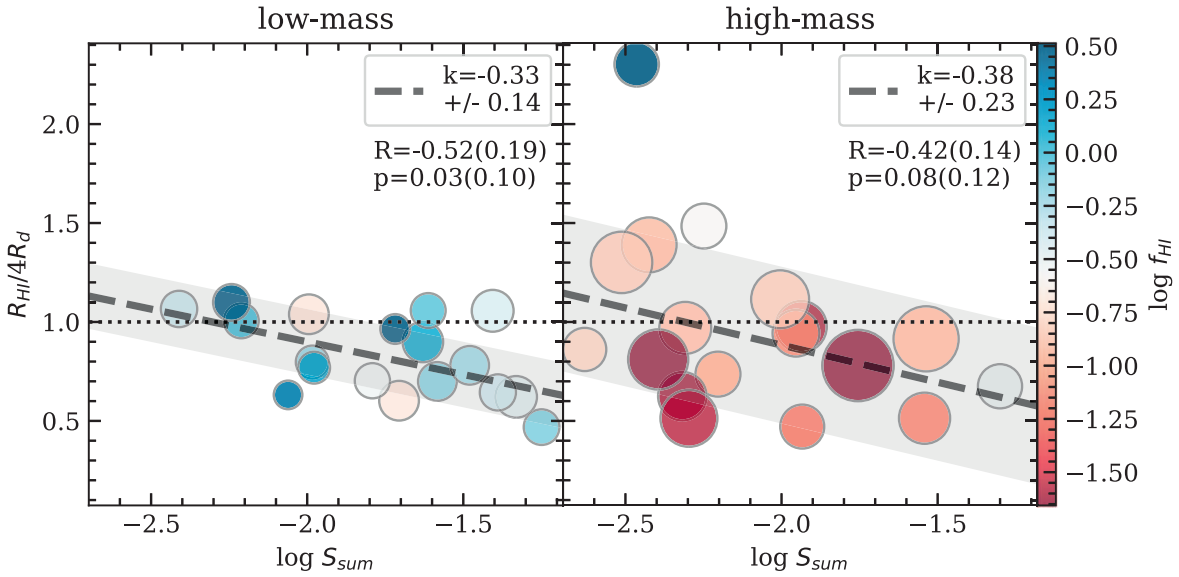


Figure 13. The correlation between the H I to optical disk size ratio (adopting $4R_d$ as the optical disk sizes) and the summed tidal parameter. The gray shaded area indicates the scatter (1σ) of data points about the linear fit. The dotted horizontal line represents $R_{\rm H\,I}/4R_d = 1$. Left: for low-mass ($\log M_*/M_\odot < 8.95$) galaxies. Right: for high-mass ($\log M_*/M_\odot > 8.95$) galaxies. The other symbols and text are the same as in Figure 3: Pearson R and p-values are shown with bootstrap errors in parentheses. Gray dashed lines are the result of a robust linear fit, with the slopes (and errors) shown in the corner. All data points are color coded by H I gas fraction (see color bar on the right). The size of data points indicates the stellar mass of the galaxy, in the sense that larger data points are used for more massive galaxies.

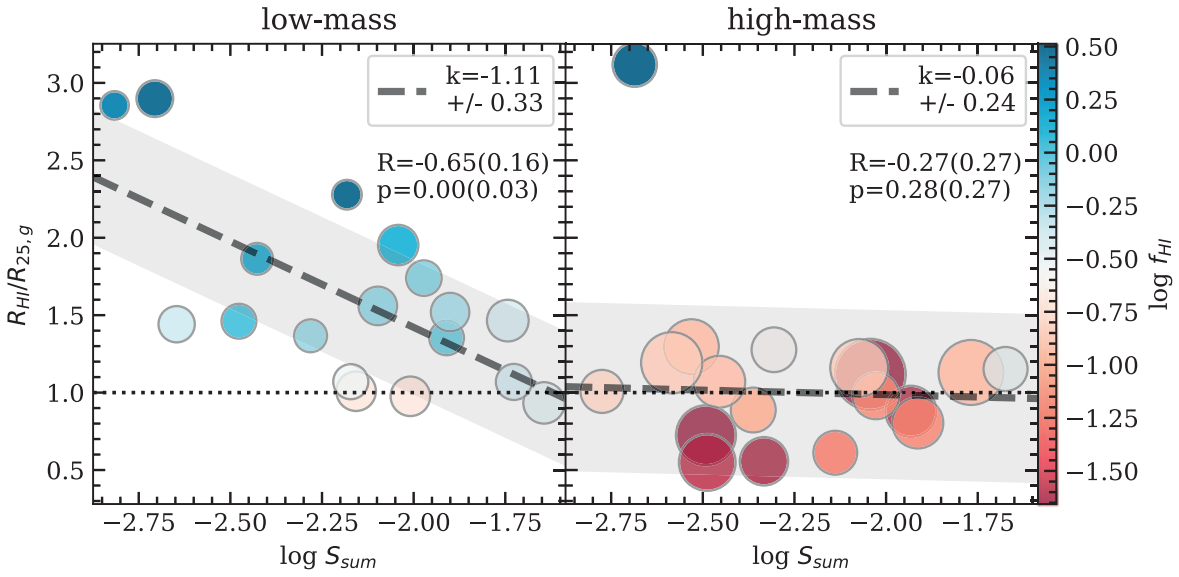


Figure 14. The correlation between the H I to optical disk size ratio (deprojection performed) and the summed tidal parameter. The gray shaded area indicates the scatter (1σ) of data points about the linear fit. The dotted horizontal line represents $R_{\rm H\,I}/R_{25,g} = 1$. Left: for low-mass ($\log M_*/M_\odot < 8.95$) galaxies. Right: for high-mass ($\log M_*/M_\odot > 8.95$) galaxies. The other symbols and text are the same as in Figure 3: Pearson R and p-values are shown with bootstrap errors in parentheses. Gray dashed lines are the result of a robust linear fit, with the slopes (and errors) shown in the corner. All data points are color coded by H I gas fraction (see color bar on the right). The size of data points indicates the stellar mass of the galaxy, in the sense that larger data points are used for more massive galaxies.

assuming exponential disks). We confirm that the results are not qualitatively different from those obtained by using $R_{25,g}$ as the estimate of disk size. We show the relation between $R_{\rm H\,I}/4R_d$ and $S_{\rm sum}$ in Figure 13, which is quite similar to that shown in Figure 4.

A.2. Correction for Projection Effect in Measuring Optical Disk Sizes

As we have mentioned in the main text, the deprojection of dwarf irregular galaxies based on photometrically derived inclinations and axis ratios could introduce large uncertainties. Previous studies also showed that the observed apparent diameter based on a surface brightness isophote is not sensitive to inclination (Tully 1972; Burstein et al. 1991; Choloniewski 1991; Bottinelli et al. 1995; but see Tully & Fouque 1985).

We confirm that most of our major results are robust against the treatment of deprojection. When deprojection is performed when deriving $R_{25,g}$, as shown in Figure 14, the H I to optical disk size ratios of high-mass galaxies are insensitive to the summed tidal parameter. All high-mass galaxies except for the merging pair (NGC 1359, ID 69) have disk size ratios close to 1, with significant scatter, though.

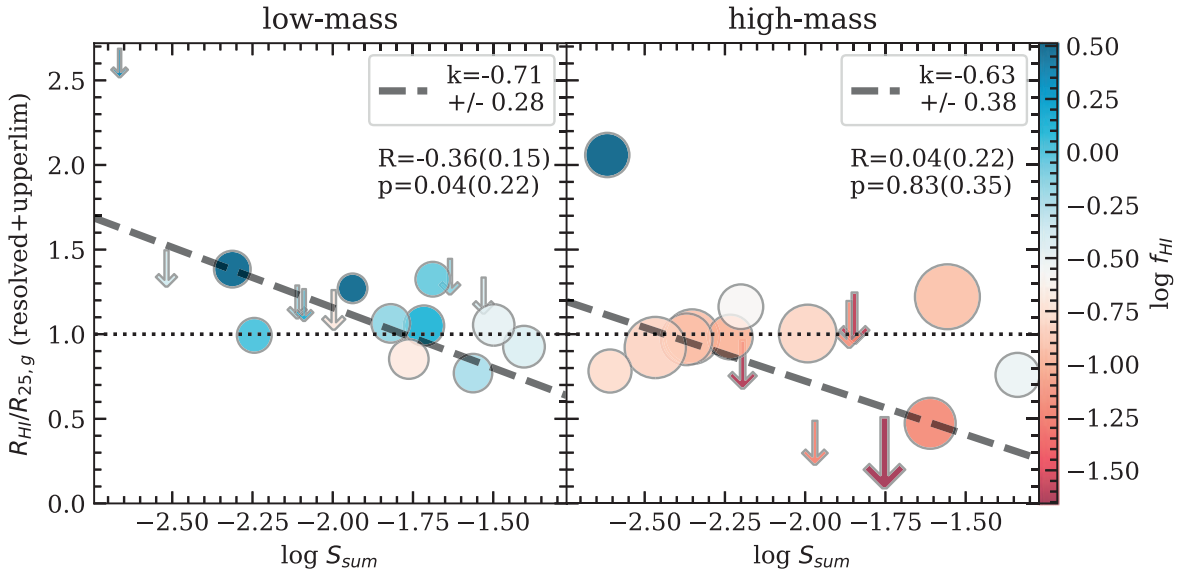


Figure 15. The correlation between the H I to optical disk size ratio (adopt directly measured H I disk sizes) and the summed tidal parameter. The dotted horizontal line represents $R_{\rm H\,I}/R_{25,g} = 1$. The downward arrows are upper limits of H I to optical disk size ratios. Left: for low-mass ($\log M_*/M_\odot < 8.95$) galaxies. Right: for high-mass ($\log M_*/M_\odot > 8.95$) galaxies. The other symbols and text are the same as in Figure 3: Kendall R and p-values are shown with bootstrap errors in parentheses. Gray dashed lines are the result of a linear fit invoking a survival analysis, with the slopes (and errors) shown in the corner. All data points are color coded by H I gas fraction (see color bar on the right). The size of data points indicates the stellar mass of the galaxy, in the sense that larger data points are used for more massive galaxies.

A.3. Measure of H I Disk Sizes

We directly measure the characteristic sizes ($R_{\rm H\,I,0}$) of the H I disks in the H I sample. The projection effect is corrected based on the axis ratios of H I disks. For 21 resolved H I disks, i.e., those with $R_{\rm H\,I,0}$ larger than $3B_{\rm maj}$ ($3'' \times 30''$), the beam smearing effect is corrected as $R_{\rm H\,I} = \sqrt{R^2_{\rm H\,I,0} - B_{\rm maj} \times B_{\rm min}}$ (Wang et al. 2016), where $R_{\rm H\,I,0}$ is the uncorrected measurement and $R_{\rm H\,I}$ is the corrected one. The sizes of the unresolved H I disks are treated as upper limits and no smearing correction is applied. We check the anticorrelation between the H I to optical disk size ratios and tidal parameter using a survival analysis (see Figure 15). If we only include resolved H I disks for such test, a Pearson R value of -0.49 and a p-value of 0.15 for the low-mass subsample is obtained (not shown in the figure).

Appendix B
Galactic Properties

We present the basic and derived galactic properties, including Petrosian magnitudes in g, r, and z band, stellar mass, and $R_{25,g}$ in Table 4. Color gradients and tidal parameters of galaxies in the H I sample are provided in Table 5. The uncertainties of $V_{\rm opt}$, grz magnitudes, $R_{25,g}$, color gradients, and tidal parameters are shown in the parentheses following. The typical uncertainty of stellar mass is $\sim$0.11 dex, which is dominated by the scatter of the stellar mass-to-light ratio as a function of $g - r$ color (Zibetti et al. 2009).

Table 4
Basic Information and Derived Quantities for All Galaxies in the Optical and H I Sample

Object ID	R.A. (deg)	Decl. (deg)	V_{opt} (km s^{-1})	References	Detected	g (mag)	r (mag)	z (mag)	$\log M_*$ ($M_\odot$)	$R_{25,g}$ (kpc)
(1)	(2)	(3)	(4)	(5)	(6)	(7)	(8)	(9)	(10)	(11)
01	51.106541	−21.544029	1588(4)	WALLABY	1	11.894(0.001)	11.242(0.001)	10.770(0.001)	10.2	150.42(0.23)
02	51.571734	−21.335320	1526(29)	NED optical	0	10.707(0.001)	9.924(0.000)	9.319(0.000)	11.0	165.07(0.09)
03	51.897030	−21.228390	1686(4)	WALLABY	1	14.264(0.003)	13.740(0.002)	13.415(0.002)	9.0	71.29(0.09)
04	53.361130	−23.712780	1810(4)	WALLABY	1	13.058(0.002)	12.439(0.001)	11.950(0.001)	9.7	69.67(0.13)
05	53.471198	−20.282588	1177(29)	NED optical	0	13.157(0.002)	12.453(0.001)	11.953(0.001)	9.9	49.89(0.19)
06	53.906212	−21.294060	1802(4)	WALLABY	1	14.341(0.003)	13.933(0.002)	13.717(0.002)	8.8	74.27(0.14)
07	54.623726	−23.027488	1701(19)	NED optical	0	10.364(0.000)	9.595(0.000)	8.991(0.000)	11.1	182.06(0.04)
08	54.878546	−18.688174	590(14)	NED optical	0	11.252(0.001)	10.490(0.001)	9.918(0.000)	10.7	103.93(0.12)
09	55.236919	−22.564470	1552(4)	WALLABY	1	11.936(0.001)	11.136(0.001)	10.559(0.001)	10.5	114.55(0.34)
10	55.704739	−22.108405	1445(6)	NED optical	0	11.840(0.001)	11.104(0.001)	10.546(0.001)	10.4	105.82(0.06)
11	55.457583	−19.581250	1914(...)	NED preferred	0	15.635(0.005)	15.060(0.004)	14.728(0.004)	8.6	22.25(0.14)
12	55.382542	−19.905139	1545(43)	NED optical	0	14.096(0.003)	13.444(0.002)	13.009(0.002)	9.4	40.60(0.07)
13	55.483667	−18.895167	2031(31)	NED optical	0	13.661(0.002)	12.970(0.002)	12.500(0.001)	9.6	46.29(0.09)
14	55.268375	−19.094444	987(45)	NED optical	0	14.885(0.004)	14.308(0.003)	13.931(0.003)	8.9	32.48(0.19)
15	55.066375	−19.081778	1614(45)	NED optical	0	14.875(0.004)	14.204(0.003)	13.751(0.002)	9.1	23.60(0.10)
16	55.180125	−18.645306	1374(45)	NED optical	−1	14.791(0.004)	14.166(0.003)	13.759(0.002)	9.0	28.58(0.28)
17	55.000333	−19.426306	1874(33)	NED optical	0	13.949(0.003)	13.257(0.002)	12.776(0.001)	9.5	34.69(0.18)
18	55.219708	−18.478000	1680(...)	NED preferred	−1	15.230(0.004)	14.560(0.003)	14.109(0.003)	9.0	22.78(0.15)
19	54.413500	−18.339472	2009(19)	NED optical	−1	12.853(0.002)	12.109(0.001)	11.547(0.001)	10.1	67.99(0.21)
20	55.288042	−18.314139	1245(41)	NED optical	−1	14.222(0.003)	13.550(0.002)	13.090(0.002)	9.4	29.87(0.17)
21	54.467369	−19.008360	1218(4)	WALLABY	1	14.249(0.003)	13.702(0.002)	13.341(0.002)	9.1	44.94(0.20)
22	54.660750	−18.427972	2127(26)	NED optical	−1	12.524(0.001)	11.785(0.001)	11.241(0.001)	10.2	71.74(0.10)
23	55.011250	−19.366610	1216(4)	WALLABY	1	14.835(0.004)	14.363(0.003)	14.089(0.003)	8.7	46.01(0.22)
24	55.029750	−18.443472	1841(30)	NED optical	−1	13.444(0.002)	12.749(0.001)	12.258(0.001)	9.7	56.13(0.18)
25	55.049333	−18.580139	1779(14)	NED optical	−1	9.966(0.000)	9.194(0.000)	8.592(0.000)	11.3	208.52(0.04)
26	55.079875	−18.931500	1693(26)	NED optical	0	13.456(0.002)	12.770(0.001)	12.277(0.001)	9.7	49.15(0.15)
27	55.251042	−19.455389	2034(...)	NED preferred	−1	15.692(0.006)	15.303(0.004)	15.089(0.004)	8.2	28.88(0.27)
28	55.436125	−18.267000	2013(47)	NED optical	−1	12.770(0.002)	12.056(0.001)	11.549(0.001)	10.0	71.15(0.09)
29	55.739125	−19.020806	1111(36)	NED optical	−1	14.313(0.003)	13.895(0.002)	13.663(0.003)	8.8	45.83(0.07)
30	54.430542	−22.908194	1515(55)	NED optical	0	14.540(0.003)	13.930(0.002)	13.511(0.002)	9.1	43.37(0.09)
31	54.568958	−22.486500	1359(45)	NED optical	0	16.101(0.006)	15.487(0.004)	15.115(0.004)	8.5	19.39(0.12)
32	53.974792	−22.139722	1374(45)	NED optical	0	15.308(0.004)	14.634(0.003)	14.181(0.003)	8.9	21.97(0.12)
33	53.938625	−21.783111	1638(45)	NED optical	0	15.682(0.005)	15.045(0.004)	14.668(0.004)	8.7	19.84(0.08)
34	53.365261	−21.564659	1509(4)	WALLABY	1	13.753(0.002)	13.102(0.002)	12.632(0.001)	9.5	30.86(0.31)
35	53.240120	−21.089420	1665(4)	WALLABY	1	14.012(0.002)	13.450(0.002)	13.121(0.002)	9.2	37.07(0.09)
36	53.012417	−20.818944	1587(10)	NED optical	0	11.674(0.001)	10.910(0.001)	10.315(0.000)	10.6	119.80(0.05)
37	54.236458	−20.589722	1689(31)	NED optical	0	15.053(0.004)	14.482(0.003)	14.101(0.002)	8.8	18.25(0.22)
38	54.162792	−20.902000	1809(30)	NED optical	0	12.970(0.001)	12.277(0.001)	11.791(0.001)	9.9	62.42(0.13)
39	55.150711	−21.525669	1644(4)	WALLABY	1	15.407(0.005)	14.987(0.004)	14.908(0.005)	8.4	32.87(0.07)
40	55.237659	−21.713140	1695(4)	WALLABY	1	14.375(0.003)	13.913(0.002)	13.607(0.002)	8.9	50.02(0.15)
41	55.860250	−21.328944	1711(45)	NED optical	0	16.308(0.007)	15.705(0.005)	15.380(0.005)	8.4	16.05(0.11)
42	55.379459	−21.681530	1644(4)	WALLABY	1	13.678(0.002)	13.045(0.002)	12.600(0.001)	9.5	79.05(0.12)
43	55.173083	−22.651139	1803(34)	NED optical	0	14.849(0.003)	14.175(0.003)	13.727(0.002)	9.1	28.87(0.07)
44	52.696541	−21.058220	1292(4)	WALLABY	1	13.748(0.002)	13.183(0.002)	12.811(0.001)	9.3	38.86(0.11)
45	53.424461	−21.478640	1859(4)	WALLABY	1	12.062(0.001)	11.557(0.001)	11.267(0.001)	9.9	88.97(0.37)
46	53.866959	−21.217030	1518(4)	WALLABY	1	15.095(0.004)	14.770(0.003)	14.611(0.003)	8.3	31.32(0.11)

Table 4
(Continued)

Object ID	R.A.	Decl.	V_{opt}	References	Detected	g	r	z	$\log M_*$	$R_{25,g}$
	(deg)	(deg)	(km s^{-1})			(mag)	(mag)	(mag)	($M_\odot$)	(kpc)
(1)	(2)	(3)	(4)	(5)	(6)	(7)	(8)	(9)	(10)	(11)
47	54.573500	−23.419167	1687(37)	NED optical	0	14.127(0.003)	13.446(0.002)	12.971(0.002)	9.4	38.73(0.05)
48	54.839291	−21.415720	1622(4)	WALLABY	1	14.921(0.004)	14.432(0.003)	14.106(0.003)	8.7	31.14(0.16)
49	54.841042	−22.724694	1495(28)	NED optical	0	12.692(0.001)	11.966(0.001)	11.413(0.001)	10.1	76.11(0.24)
50	55.311790	−23.836941	1885(4)	WALLABY	1	13.236(0.002)	12.668(0.001)	12.307(0.001)	9.5	60.66(0.28)
51	55.909050	−21.237700	1612(4)	WALLABY	1	14.933(0.004)	14.480(0.003)	14.304(0.003)	8.6	49.50(0.10)
52	56.208125	−21.920556	1670(10)	NED optical	0	11.642(0.001)	10.915(0.001)	10.437(0.001)	10.5	102.29(0.03)
53	54.921719	−23.844400	1622(4)	WALLABY	1	16.179(0.006)	15.883(0.006)	15.784(0.007)	7.8	27.41(0.11)
54	55.170792	−22.287060	1774(4)	WALLABY	1	15.273(0.004)	14.757(0.003)	14.427(0.003)	8.6	48.36(0.12)
55	55.578350	−22.752560	1569(4)	WALLABY	1	14.635(0.003)	14.130(0.002)	13.909(0.003)	8.9	46.92(0.06)
56	50.777500	−21.375194	1597(26)	NED optical	−1	12.872(0.001)	12.159(0.001)	11.633(0.001)	10.0	56.13(0.08)
57	51.469250	−21.289056	1428(45)	NED optical	0	15.064(0.004)	14.332(0.003)	13.790(0.002)	9.1	14.16(0.23)
58	51.925667	−21.699611	1295(...)	NED preferred	0	15.356(0.004)	14.720(0.003)	14.287(0.003)	8.8	34.31(0.15)
59	51.202083	−21.336528	1333(60)	NED optical	0	13.002(0.002)	12.459(0.001)	12.105(0.001)	9.6	63.81(0.02)
60	51.230431	−21.783890	1456(4)	WALLABY	1	15.611(0.005)	15.128(0.004)	14.885(0.004)	8.4	30.28(0.07)
61	51.630583	−21.216806	1548(45)	NED optical	0	14.501(0.003)	13.776(0.002)	13.217(0.002)	9.4	22.60(0.23)
62	56.321789	−23.002470	1546(4)	WALLABY	1	12.751(0.001)	12.053(0.001)	11.533(0.001)	10.0	65.52(0.23)
63	56.344791	−24.202419	1733(4)	WALLABY	1	16.931(0.010)	16.549(0.008)	16.441(0.014)	7.7	12.88(0.03)
64	56.235859	−23.699699	1819(4)	WALLABY	1	15.363(0.004)	14.920(0.004)	14.686(0.004)	8.4	23.49(0.13)
65	57.058670	−21.474470	1586(4)	WALLABY	1	12.962(0.002)	12.308(0.001)	11.912(0.001)	9.8	74.14(0.20)
66	56.145222	−21.192070	1578(4)	WALLABY	1	15.721(0.005)	15.258(0.004)	15.038(0.004)	8.3	26.27(0.13)
67	52.252880	−22.146580	1627(4)	WALLABY	1	14.479(0.003)	13.920(0.002)	13.598(0.002)	9.0	41.78(0.12)
68	52.422920	−22.285000	1755(4)	WALLABY	1	13.540(0.002)	13.134(0.002)	12.898(0.002)	9.1	41.44(0.10)
69	53.448792	−19.492060	1964(4)	WALLABY	1	12.543(0.001)	12.345(0.001)	12.303(0.001)	9.1	58.47(0.03)
70	54.370201	−24.500299	1497(4)	WALLABY	1	11.196(0.001)	10.769(0.001)	10.522(0.001)	10.1	113.29(0.19)
71	52.409611	−23.350330	1657(4)	WALLABY	1	15.426(0.004)	15.031(0.004)	14.801(0.004)	8.3	39.80(0.13)
72	53.117611	−23.380930	1755(4)	WALLABY	1	15.772(0.005)	15.398(0.004)	15.203(0.005)	8.1	23.06(0.14)
73	52.134258	−22.501329	1774(4)	WALLABY	1	16.084(0.006)	15.699(0.005)	15.490(0.005)	8.0	33.97(0.16)
74	53.259392	−24.132870	1915(4)	WALLABY	1	14.938(0.004)	14.558(0.003)	14.354(0.003)	8.5	61.93(0.18)
75	54.072398	−25.604380	1590(4)	WALLABY	1	14.552(0.003)	14.005(0.002)	13.636(0.002)	9.0	44.32(0.13)

Note. Column (1): Object ID. Columns (2)–(3): R.A. and decl. (J2000). Column (4): optical velocity $V_{opt} = cz$, where c is the speed of light and z is the redshift. Column (5): the reference of V_{opt}. Column (6): whether it is detected by WALLABY: -1 = not in the footprint; 0 = not detected; 1 = detected. Columns (7)–(9): Petrosian magnitude in g, r, and z band. Column (10): derived stellar mass; see text in Section 3.1.2. Column (11): optical disk size measured in g band at 25 mag arcsec^{-2} isophote; see text in Section 3.1.2.

Table 5
Identifications and Derived Quantities for Galaxies in the H I Sample

Object ID	WALLABY ID	Other ID	CG_{01} (mag $R_{50,z}^{-1}$)	CG_{12} (mag $R_{50,z}^{-1}$)	S_{sum}	$S_{strongest}$	$S_{nearest}$
(1)	(2)	(3)	(4)	(5)	(6)	(7)	(8)
01	J032425-213233	NGC 1325	−0.03(0.01)	−0.10(0.01)	−1.56(0.16)	−1.76(0.23)	−2.51(0.45)
03	J032735-211339	ESO 548-21	−0.08(0.01)	0.00(0.01)	−1.34(0.20)	−1.44(0.25)	−3.03(0.33)
04	J033326-234246	IC 1952	−0.16(0.01)	0.04(0.03)	−2.35(0.11)	−2.75(0.24)	−3.85(0.19)
06	J033537-211742	IC 1962	0.00(0.01)	−0.06(0.01)	−1.72(0.10)	−2.37(0.16)	−2.45(0.46)
09	J034056-223350	NGC 1415	−0.16(0.05)	−0.05(0.00)	−1.78(0.12)	−2.36(0.31)	−2.38(0.26)
21	J033752-190024	NGC 1390	−0.06(0.01)	0.04(0.01)	−2.23(0.43)	−2.59(0.86)	−2.98(1.04)
23	J034002-192200	ESO 548-65	−0.04(0.02)	0.00(0.01)	−1.76(0.47)	−1.98(0.75)	−1.98(0.75)
34	J033327-213352	ESO 548-36	−0.11(0.09)	0.16(0.02)	−1.87(0.38)	−2.03(0.56)	−2.03(0.56)
35	J033257-210513	ESO 548-34	−0.12(0.02)	0.04(0.01)	−1.88(0.14)	−2.15(0.24)	−2.15(0.24)
39	J034036-213129	ESO 548-69	0.04(0.02)	0.10(0.03)	−1.65(0.05)	−2.11(0.10)	−2.44(0.13)
40	J034057-214245	NGC 1414	−0.08(0.01)	−0.04(0.01)	−1.40(0.09)	−1.62(0.14)	−1.62(0.14)
42	J034131-214051	NGC 1422	−0.26(0.01)	−0.03(0.01)	−1.61(0.08)	−2.07(0.17)	−2.07(0.17)
44	J033047-210333	ESO 548-29	−0.07(0.01)	−0.00(0.01)	−2.22(0.24)	−2.45(0.40)	−2.45(0.40)
45	J033341-212844	IC 1953	−0.24(0.01)	−0.03(0.02)	−1.99(0.23)	−2.38(0.55)	−2.38(0.55)
46	J033527-211302	ESO 548-49	−0.09(0.01)	−0.06(0.01)	−1.69(0.22)	−2.01(0.46)	−2.01(0.46)
48	J033921-212450	LEDA 13460	−0.00(0.02)	0.07(0.02)	−2.01(0.04)	−2.82(0.16)	−3.18(0.11)
50	J034114-235017	ESO 482-35	−0.07(0.03)	0.01(0.00)	−2.37(0.18)	−2.66(0.33)	−3.97(0.43)
51	J034337-211418	ESO 549-6	−0.05(0.01)	−0.02(0.01)	−1.82(0.05)	−2.45(0.14)	−2.73(0.19)
53	J033941-235054	ESO 482-27	0.04(0.04)	0.07(0.01)	−1.94(0.09)	−2.23(0.15)	−3.14(0.43)
54	J034040-221711	ESO 548-70	−0.02(0.02)	−0.03(0.00)	−1.56(0.16)	−1.97(0.37)	−1.97(0.37)
55	J034219-224520	ESO 482-36	−0.10(0.01)	−0.01(0.01)	−1.50(0.08)	−1.75(0.12)	−1.75(0.12)
60	J032455-214701	ESO 548-11	−0.09(0.01)	−0.01(0.01)	−1.55(0.13)	−1.84(0.23)	−1.84(0.23)
62	J034517-230001	NGC 1438	−0.14(0.03)	−0.08(0.02)	−2.36(0.09)	−3.05(0.19)	−4.68(0.45)
63	J034522-241208	LEDA 79249	0.22(0.05)	0.30(0.07)	−2.68(0.05)	−3.02(0.10)	−4.19(0.16)
64	J034456-234158	LEDA 13743	0.03(0.04)	0.30(0.03)	−2.53(0.09)	−3.02(0.21)	−4.46(0.17)
65	J034814-212824	ESO 549-18	−0.03(0.01)	−0.03(0.01)	−2.40(0.08)	−2.90(0.21)	−4.41(0.18)
66	J034434-211123	LEDA 13511	0.02(0.01)	0.06(0.01)	−1.96(0.05)	−2.56(0.10)	−2.56(0.10)
67	J032900-220851	ESO 548-25	0.07(0.03)	−0.00(0.02)	−1.99(0.07)	−2.49(0.17)	−2.73(0.23)
68	J032941-221642	NGC 1347	−0.20(0.02)	0.02(0.02)	−2.20(0.08)	−2.86(0.24)	−2.86(0.24)
69	J033347-192946	NGC 1359	−0.24(0.09)	−0.06(0.03)	−2.62(0.15)	−3.07(0.35)	−4.26(1.20)
70	J033728-243010	NGC 1385	−0.08(0.02)	0.02(0.03)	−2.47(0.14)	−2.91(0.36)	−4.39(0.27)
71	J032937-232103	ESO 481-30	−0.01(0.01)	−0.03(0.03)	−2.24(0.05)	−2.76(0.12)	−4.20(0.18)
72	J033228-232245	ESO 482-3	0.08(0.02)	0.08(0.01)	−2.12(0.06)	−2.59(0.12)	−2.59(0.12)
73	J032831-222957	ESO 481-28	0.04(0.03)	0.16(0.02)	−2.10(0.07)	−2.70(0.09)	−2.70(0.09)
74	J033302-240756	ESO 482-5	−0.05(0.01)	−0.11(0.01)	−2.31(0.13)	−2.66(0.21)	−2.66(0.21)
75	J033617-253615	ESO 482-11	−0.06(0.01)	−0.04(0.01)	−2.61(0.07)	−3.18(0.19)	−3.18(0.19)

Note. Column (1): Object ID. Column (2): WALLABY identifier. Column (3): other identification. Columns (4)–(5): color gradients in $R < R_{50,z}$ and $R_{50,z} < R < 2R_{50,z}$. Columns (6)–(8): tidal parameters of the summed, the strongest, and the nearest perturber.

Appendix C
Atlas

We present the optical color images and color profiles for galaxies in the H I sample in Figure 16. The foreground stars are masked. For each galaxy, we show $g-r$, $g-z$, and $r-z$ profiles, respectively. CG_{01} and CG_{12} are also shown along with the $g-r$ profile.

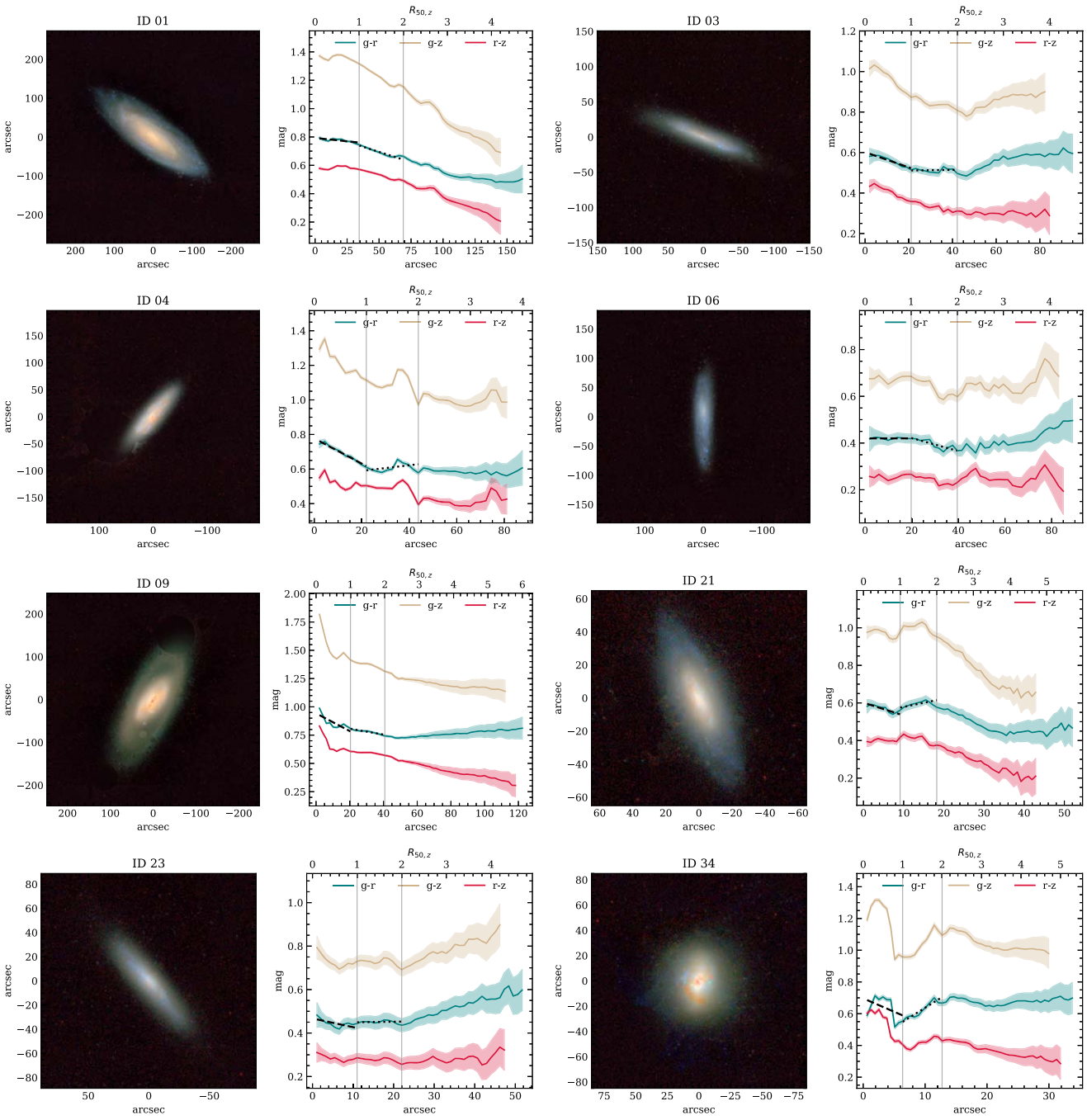


Figure 16. The optical color images (left panel) and color profiles (right panel) for galaxies in the H I sample. The $g-r$, $g-z$, and $r-z$ profiles are shown in green, yellow, and red, respectively. The shaded area indicates the uncertainties of the profile. The fitted linear lines with slopes equal to CG_{01} and CG_{12} are shown as black dashed and dotted lines overlapping on the $g-r$ profile. The gray vertical lines indicate $1R_{50,z}$ and $2R_{50,z}$.

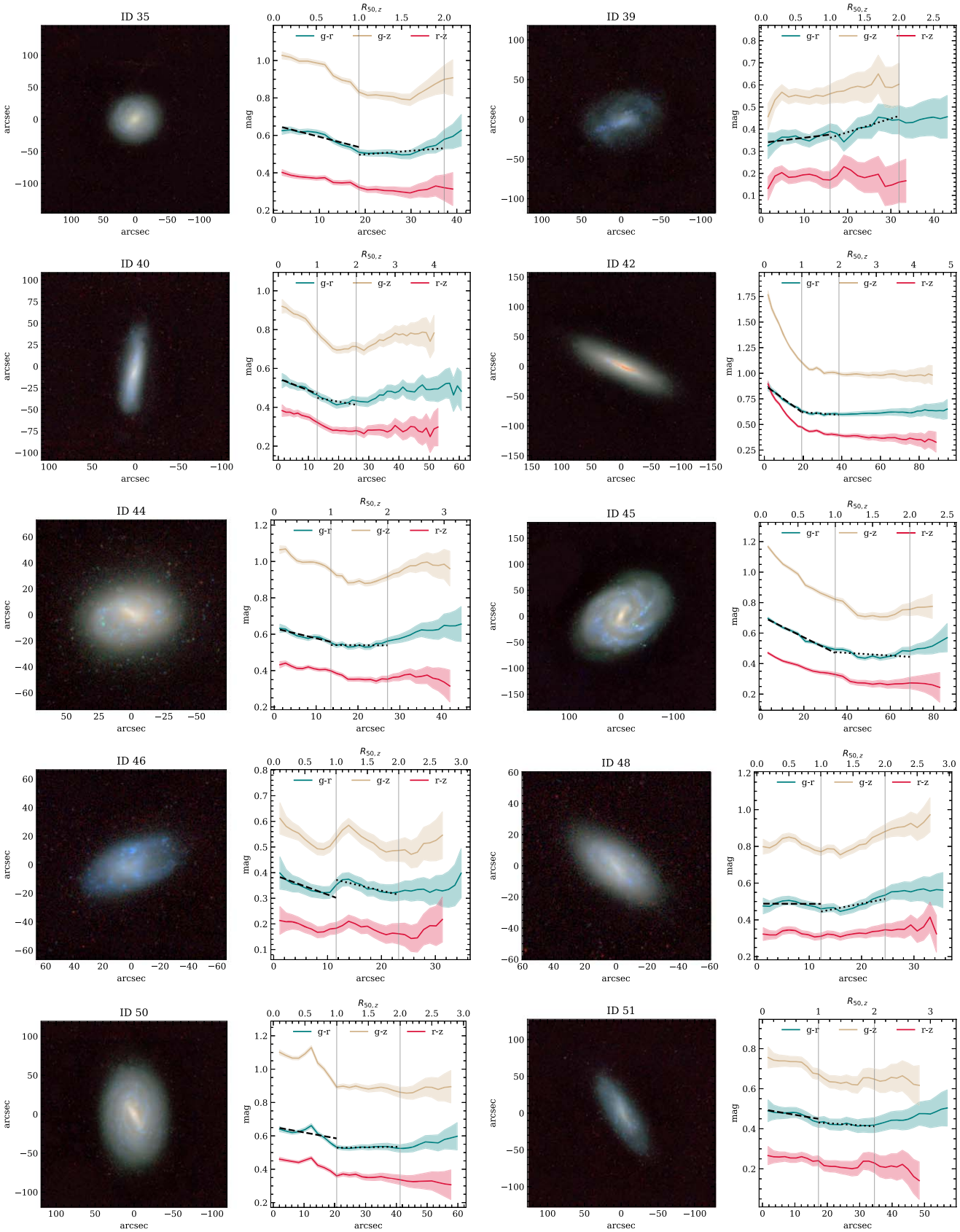


Figure 16. (Continued.)

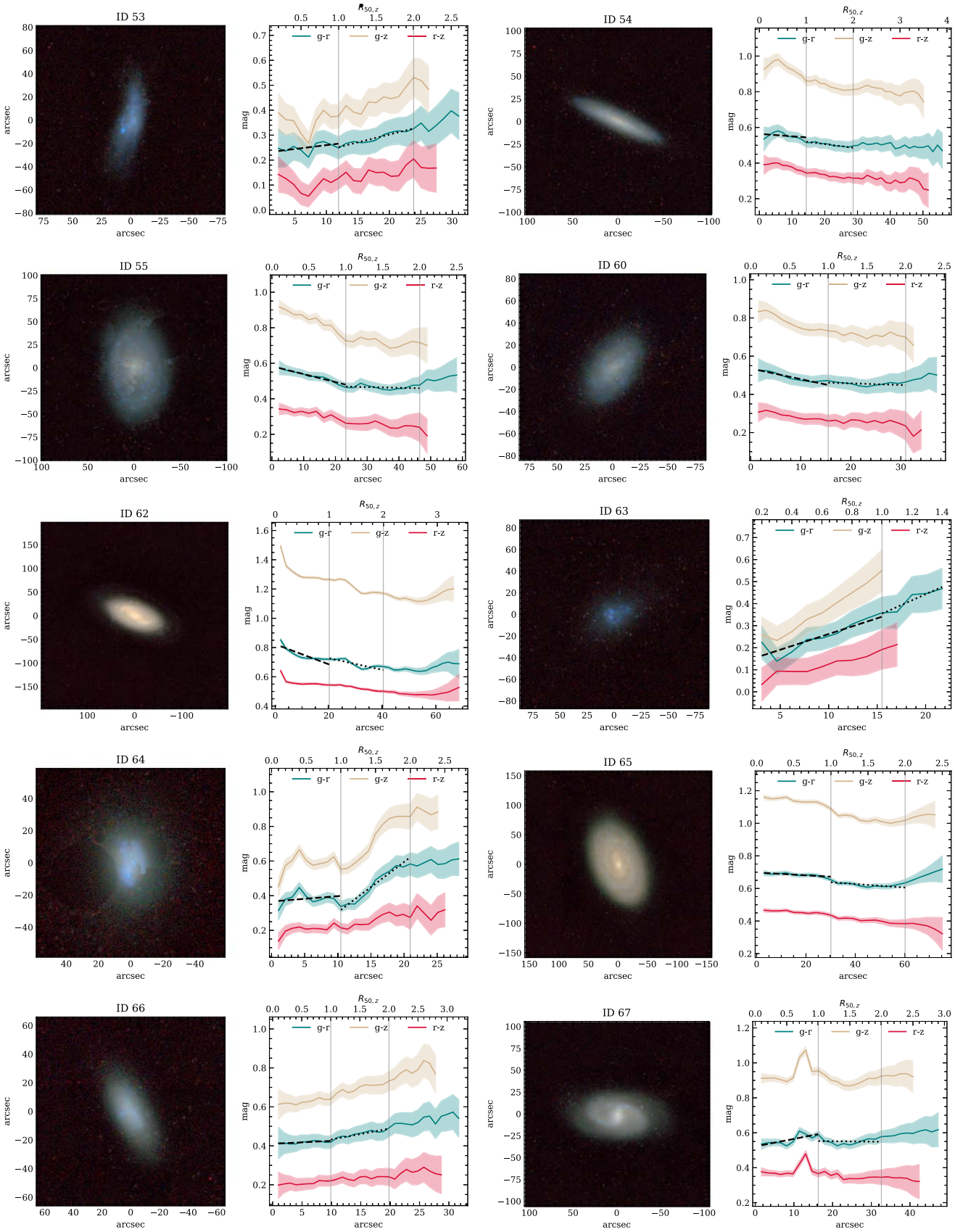


Figure 16. (Continued.)

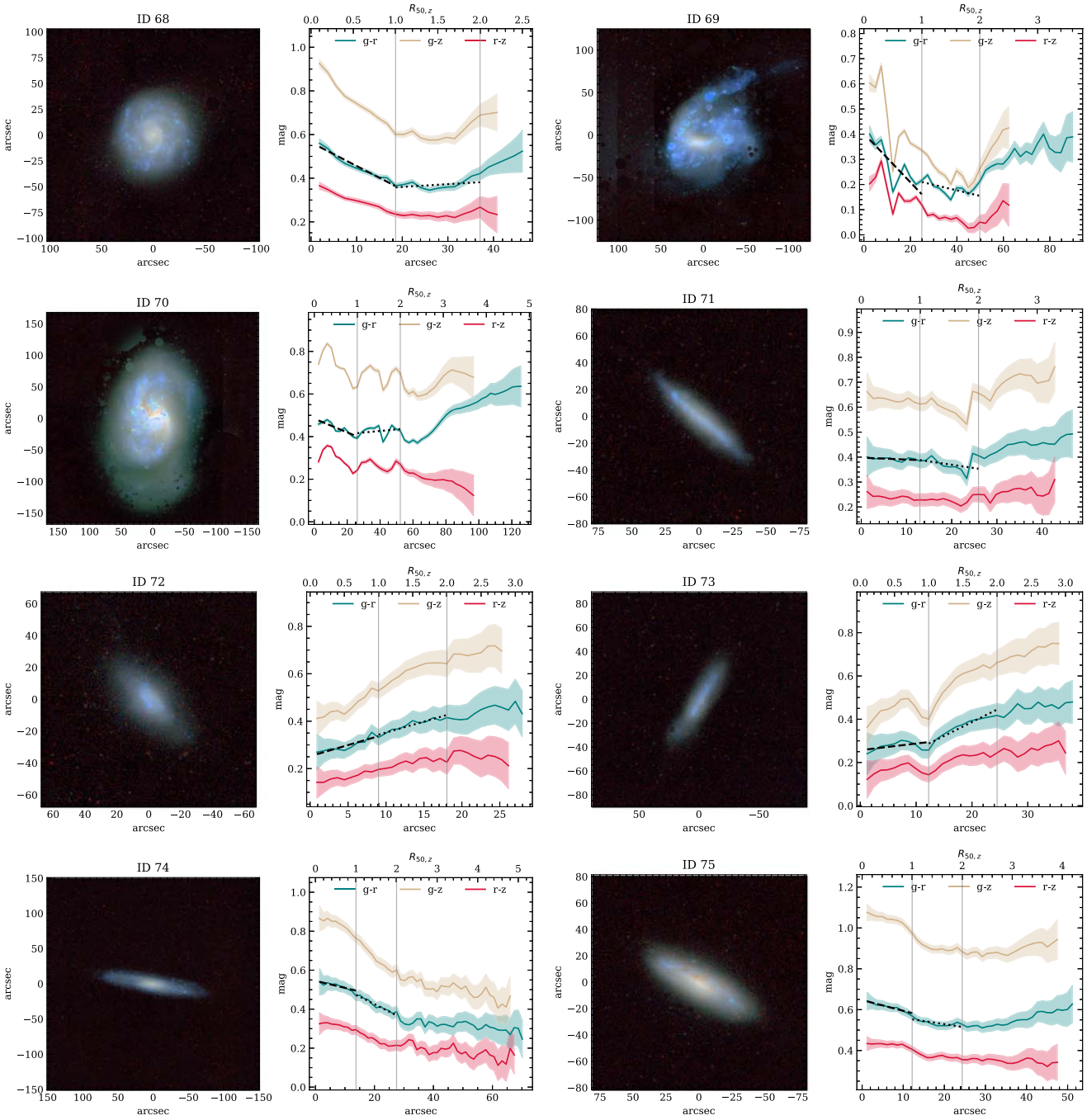


Figure 16. (Continued.)

ORCID iDs

Shun Wang https://orcid.org/0000-0002-9663-3384
Jing Wang https://orcid.org/0000-0002-6593-8820
Bumhyun Lee https://orcid.org/0000-0002-3810-1806
T. N. Reynolds https://orcid.org/0000-0002-6606-5953
L. Staveley-Smith https://orcid.org/0000-0002-8057-0294
Li Shao https://orcid.org/0000-0003-2015-777X
O. I. Wong https://orcid.org/0000-0003-4264-3509
B. Catinella https://orcid.org/0000-0002-7625-562X
L. Verdes-Montenegro https://orcid.org/0000-0003-0156-6180
B. S. Koribalski https://orcid.org/0000-0003-4351-993X
D. Kleiner https://orcid.org/0000-0002-7573-555X
J. Rhee https://orcid.org/0000-0001-8496-4306
F. Bigiel https://orcid.org/0000-0003-0166-9745
B. W. Holwerda https://orcid.org/0000-0002-4884-6756
S.-H. Oh https://orcid.org/0000-0002-8379-0604
K. Spekkens https://orcid.org/0000-0002-0956-7949

References

Abergel, A., Ade, P. A. R., Aghanim, N., et al. 2014, A&A, 571, A11
Alonso, M. S., Tissera, P. B., Coldwell, G., & Lambas, D. G. 2004, MNRAS, 352, 1081
Argudo-Fernández, M., Verley, S., Bergond, G., et al. 2014, A&A, 564, A94
Argudo-Fernández, M., Verley, S., Bergond, G., et al. 2015, A&A, 578, A110
Bacchini, C., Fraternali, F., Iorio, G., et al. 2020, A&A, 641, A70
Bakos, J., Trujillo, I., & Pohlen, M. 2008, ApJL, 683, L103
Balogh, M. L., Navarro, J. F., & Morris, S. L. 2000, ApJ, 540, 113

Barnes, J. E., & Hernquist, L. 1996, ApJ, 471, 115
Barnes, J. E., & Hernquist, L. E. 1991, ApJL, 370, L65
Barton Gillespie, E., Geller, M. J., & Kenyon, S. J. 2003, ApJ, 582, 668
Behroozi, P., Wechsler, R. H., Hearin, A. P., & Conroy, C. 2019, MNRAS, 488, 3143
Belfiore, F., Maiolino, R., Bundy, K., et al. 2018, MNRAS, 477, 3014
Bell, E. F., & de Jong, R. S. 2000, MNRAS, 312, 497
Bertin, E., & Arnouts, S. 1996, A&AS, 117, 393
Bigiel, F., Leroy, A., Walter, F., et al. 2008, AJ, 136, 2846
Bok, J., Skelton, R. E., Cluver, M. E., et al. 2020, MNRAS, 499, 3193
Boselli, A., & Gavazzi, G. 2006, PASP, 118, 517
Boselli, A., & Gavazzi, G. 2014, A&ARv, 22, 74
Boselli, A., Voyer, E., Boissier, S., et al. 2014, A&A, 570, A69
Bottinelli, L., Gouguenheim, L., Paturel, G., & Teerikorpi, P. 1995, A&A, 296, 64
Bradley, L., Sipocz, B., Robitaille, T., et al. 2016, Photutils: Photometry tools, Astrophysics Source Code Library, ascl:1609.011
Broeils, A. H., & Rhee, M. H. 1997, A&A, 324, 877
Brough, S., Forbes, D. A., Kilborn, V. A., Couch, W., & Colless, M. 2006, MNRAS, 369, 1351
Brown, T., Catinella, B., Cortese, L., et al. 2017, MNRAS, 466, 1275
Burgett, W. S., Vick, M. M., Davis, D. S., et al. 2004, MNRAS, 352, 605
Burstein, D., Haynes, M. P., & Faber, M. 1991, Natur, 353, 515
Bustamante, S., Ellison, S. L., Patton, D. R., & Sparre, M. 2020, MNRAS, 494, 3469
Bustamante, S., Sparre, M., Springel, V., & Grand, R. J. J. 2018, MNRAS, 479, 3381
Byrd, G., & Valtonen, M. 1990, ApJ, 350, 89
Calzetti, D., Armus, L., Bohlin, R. C., et al. 2000, ApJ, 533, 682
Cao, C., Xu, C. K., Domingue, D., et al. 2016, ApJS, 222, 16
Cardelli, J. A., Clayton, G. C., & Mathis, J. S. 1989, ApJ, 345, 245
Catinella, B., Saintonge, A. A., Janowiecki, S., et al. 2018, MNRAS, 476, 875
Choloniewski, J. 1991, MNRAS, 250, 486
Chown, R., Li, C., Athanassoula, E., et al. 2019, MNRAS, 484, 5192
Chung, A., van Gorkom, J. H., Kenney, J. D. P., Crowl, H., & Vollmer, B. 2009, AJ, 138, 1741
Cibinel, A., Carollo, C. M., Lilly, S. J., et al. 2013, ApJ, 777, 116
Cortese, L., Catinella, B., & Smith, R. 2021, PASA, 38, e035
Cox, T. J., Jonsson, P., Somerville, R. S., Primack, J. R., & Dekel, A. 2008, MNRAS, 384, 386
Cox, T. J., Primack, J., Jonsson, P., & Somerville, R. S. 2004, ApJL, 607, L87
Croton, D. J., Springel, V., White, S. D. M., et al. 2006, MNRAS, 365, 11
de Jong, R. S. 1996, A&A, 313, 377
Dekel, A., & Burkert, A. 2014, MNRAS, 438, 1870
Dey, A., Schlegel, D. J., Lang, D., et al. 2019, AJ, 157, 168
El-Badry, K., Wetzel, A., Geha, M., et al. 2016, ApJ, 820, 131
Ellison, S. L., Catinella, B., & Cortese, L. 2018a, MNRAS, 478, 3447
Ellison, S. L., Fertig, D., Rosenberg, J. L., et al. 2015, MNRAS, 448, 221
Ellison, S. L., Patton, D. R., Mendel, J. T., & Scudder, J. M. 2011, MNRAS, 418, 2043
Ellison, S. L., Patton, D. R., Simard, L., & McConnachie, A. W. 2008, AJ, 135, 1877
Ellison, S. L., Patton, D. R., Simard, L., et al. 2010, MNRAS, 407, 1514
Ellison, S. L., Sánchez, S. F., Ibarra-Medel, H., et al. 2018b, MNRAS, 474, 2039
Elmegreen, B. G., Struck, C., & Hunter, D. A. 2014, ApJ, 796, 110
English, J., Koribalski, B., Bland-Hawthorn, J., Freeman, K. C., & McCain, C. F. 2010, AJ, 139, 102
Espada, D., Verdes-Montenegro, L., Huchtmeier, W. K., et al. 2011, A&A, 532, A117
Fabello, S., Kauffmann, G., Catinella, B., et al. 2012, MNRAS, 427, 2841
Feigelson, E. D., & Nelson, P. I. 1985, ApJ, 293, 192
Fernández Lorenzo, M., Sulentic, J., Verdes-Montenegro, L., et al. 2014, ApJL, 788, L39
For, B. Q., Staveley-Smith, L., Westmeier, T., et al. 2019, MNRAS, 489, 5723
For, B. Q., Wang, J., Westmeier, T., et al. 2021, MNRAS, 507, 2300
Forbes, D. A., Sanchez-Blazquez, P., Phan, A. T. T., et al. 2006, MNRAS, 366, 1230
Fujita, Y. 1998, ApJ, 509, 587
Gadotti, D. A., & dos Anjos, S. 2001, AJ, 122, 1298
Gao, L., White, S. D. M., Jenkins, A., Stoehr, F., & Springel, V. 2004, MNRAS, 355, 819
Gavazzi, G., Boselli, A., van Driel, W., & O'Neil, K. 2005, A&A, 429, 439
Gavazzi, G., O'Neil, K., Boselli, A., & van Driel, W. 2006, A&A, 449, 929
Gavazzi, G., Savorgnan, G., Fossati, M., et al. 2013, A&A, 553, A90
Gnedin, O. Y. 2003, ApJ, 582, 141
Gonzalez-Perez, V., Castander, F. J., & Kauffmann, G. 2011, MNRAS, 411, 1151
Gunn, J. E., & Gott, J. R. 1972, ApJ, 176, 1
Guo, H., Jones, M. G., Wang, J., & Lin, L. 2021, ApJ, 918, 53
Haines, C. P., Pereira, M. J., Smith, G. P., et al. 2015, ApJ, 806, 101
Hani, M. H., Gosain, H., Ellison, S. L., Patton, D. R., & Torrey, P. 2020, MNRAS, 493, 3716
Haynes, M. P., Giovanelli, R., Martin, A. M., et al. 2011, AJ, 142, 170
Henriksen, M., & Byrd, G. 1996, ApJ, 459, 82
Hernquist, L., & Mihos, J. C. 1995, ApJ, 448, 41
Hess, K. M., & Wilcots, E. M. 2013, AJ, 146, 124
Hibbard, J. E., van der Hulst, J. M., Barnes, J. E., & Rich, R. M. 2001, AJ, 122, 2969
Hibbard, J. E., & van Gorkom, J. H. 1996, AJ, 111, 655
Holwerda, B. W., Pirzkal, N., de Blok, W. J. G., et al. 2011, MNRAS, 416, 2401
Hopkins, P. F., Cox, T. J., Hernquist, L., et al. 2013, MNRAS, 430, 1901
Hopkins, P. F., Cox, T. J., Younger, J. D., & Hernquist, L. 2009, ApJ, 691, 1168
Hunter, D. A., Ficut-Vicas, D., Ashley, T., et al. 2012, AJ, 144, 134
Isobe, T., Feigelson, E. D., & Nelson, P. I. 1986, ApJ, 306, 490
Jackson, R. A., Kaviraj, S., Martin, G., et al. 2021, MNRAS, 502, 1785
Kampczyk, P., Lilly, S. J., de Ravel, L., et al. 2013, ApJ, 762, 43
Karachentsev, I. D., Makarov, D. I., & Kaisina, E. I. 2013, AJ, 145, 101
Kauffmann, G. 2015, MNRAS, 454, 1840
Kauffmann, G., Li, C., Zhang, W., & Weinmann, S. 2013, MNRAS, 430, 1447
Kauffmann, G., White, S. D. M., Heckman, T. M., et al. 2004, MNRAS, 353, 713
Kewley, L. J., Geller, M. J., & Barton, E. J. 2006, AJ, 131, 2004
Kewley, L. J., Rupke, D., Zahid, H. J., Geller, M. J., & Barton, E. J. 2010, ApJL, 721, L48
Kilborn, V. A., Forbes, D. A., Barnes, D. G., et al. 2009, MNRAS, 400, 1962
Koopmann, R. A., & Kenney, J. D. P. 2004, ApJ, 613, 866
Koribalski, B. S., & López-Sánchez, Á. R. 2009, MNRAS, 400, 1749
Koribalski, B. S., Staveley-Smith, L., Westmeier, T., et al. 2020, Ap&SS, 365, 118
Lambas, D. G., Tissera, P. B., Alonso, M. S., & Coldwell, G. 2003, MNRAS, 346, 1189
Larson, R. B., & Tinsley, B. M. 1978, ApJ, 219, 46
Lavalley, M., Isobe, T., & Feigelson, E. 1992, in ASP Conf. Ser. 25, Astronomical Data Analysis Software and Systems I, ed. D. M. Worrall, C. Biemesderfer, & J. Barnes (San Francisco, CA: ASP), 245
Lee-Waddell, K., Koribalski, B. S., Westmeier, T., et al. 2019, MNRAS, 487, 5248
Leroy, A. K., Walter, F., Brinks, E., et al. 2008, AJ, 136, 2782
Lisenfeld, U., Alatalo, K., Zucker, C., et al. 2017, A&A, 607, A110
Lisenfeld, U., Espada, D., Verdes-Montenegro, L., et al. 2011, A&A, 534, A102
Lisenfeld, U., Verdes-Montenegro, L., Sulentic, J., et al. 2007, A&A, 462, 507
MacArthur, L. A., Courteau, S., Bell, E., & Holtzman, J. A. 2004, ApJS, 152, 175
Maddox, N., Hess, K. M., Obreschkow, D., Jarvis, M. J., & Blyth, S. L. 2015, MNRAS, 447, 1610
Manuwal, A., Ludlow, A. D., Stevens, A. R. H., Wright, R. J., & Robotham, A. S. G. 2022, MNRAS, 510, 3408
Marino, R. A., Gil De Paz, A., Sánchez, S. F., et al. 2016, A&A, 585, A47
Markevitch, M., & Vikhlinin, A. 2007, PhR, 443, 1
Martin, D. C., Fanson, J., Schiminovich, D., et al. 2005, ApJL, 619, L1
Martinez-Badenes, V., Lisenfeld, U., Espada, D., et al. 2012, A&A, 540, A96
Mayer, L., Governato, F., Colpi, M., et al. 2001, ApJL, 547, L123
McGaugh, S. S., Schombert, J. M., Bothun, G. D., & de Blok, W. J. G. 2000, ApJL, 533, L99
Merloni, A., Predehl, P., Becker, W., et al. 2012, arXiv:1209.3114
Mihos, J. C., & Hernquist, L. 1994, ApJL, 431, L9
Mihos, J. C., Richstone, D. O., & Bothun, G. D. 1992, ApJ, 400, 153
Mo, H. J., Mao, S., & White, S. D. M. 1998, MNRAS, 295, 319
Moore, B., Katz, N., Lake, G., Dressler, A., & Oemler, A. 1996, Natur, 379, 613
Moore, B., Lake, G., Quinn, T., & Stadel, J. 1999, MNRAS, 304, 465
Morales-Vargas, A., Torres-Papaqui, J. P., Rosales-Ortega, F. F., et al. 2020, MNRAS, 499, 4370
Moreno, J., Torrey, P., Ellison, S. L., et al. 2021, MNRAS, 503, 3113
Muñoz-Mateos, J. C., Gil de Paz, A., Boissier, S., et al. 2007, ApJ, 658, 1006
Murugeshan, C., Kilborn, V. A., For, B. Q., et al. 2021, MNRAS, 507, 2949
Nipoti, C., & Binney, J. 2007, MNRAS, 382, 1481
Nulsen, P. E. J. 1982, MNRAS, 198, 1007

Oh, S. H., Kim, W., Lee, H. M., & Kim, J. 2008, ApJ, 683, 94
Oman, K. A., Marasco, A., Navarro, J. F., et al. 2019, MNRAS, 482, 821
Omar, A., & Dwarakanath, K. S. 2005, JApA, 26, 1
Pan, H.-A., Lin, L., Hsieh, B.-C., et al. 2018, ApJ, 868, 132
Pan, H.-A., Lin, L., Hsieh, B.-C., et al. 2019, ApJ, 881, 119
Pan, Z., Li, J., Lin, W., et al. 2015, ApJL, 804, L42
Pan, Z., Zheng, X., Lin, W., et al. 2016, ApJ, 819, 91
Park, C., & Choi, Y.-Y. 2005, ApJL, 635, L29
Patton, D. R., Wilson, K. D., Metrow, C. J., et al. 2020, MNRAS, 494, 4969
Pearson, S., Besla, G., Putman, M. E., et al. 2016, MNRAS, 459, 1827
Peng, Y.-j., Lilly, S. J., Kovač, K., et al. 2010, ApJ, 721, 193
Perez, J., Tissera, P., Padilla, N., Alonso, M. S., & Lambas, D. G. 2009, MNRAS, 399, 1157
Reynolds, T. N., Westmeier, T., Staveley-Smith, L., et al. 2019, MNRAS, 482, 3591
Reynolds, T. N., Westmeier, T., & Staveley-Smith, L. 2020, MNRAS, 499, 3233
Reynolds, T. N., Westmeier, T., Staveley-Smith, L., Chauhan, G., & Lagos, C. D. P. 2020, MNRAS, 493, 5089
Rix, H.-W., Barden, M., Beckwith, S. V. W., et al. 2004, ApJS, 152, 163
Rupke, D. S. N., Kewley, L. J., & Barnes, J. E. 2010, ApJL, 710, L156
Sabater, J., Leon, S., Verdes-Montenegro, L., et al. 2008, A&A, 486, 73
Saintonge, A., Catinella, B., Cortese, L., et al. 2016, MNRAS, 462, 1749
Sánchez-Janssen, R., Méndez-Abreu, J., & Aguerri, J. A. L. 2010, MNRAS, 406, L65
Sandage, A., & Bedke, J. 1994, The Carnegie atlas of Galaxies (Washington, DC: Carnegie Institution of Washington), 638
Scott, T. C., Sengupta, C., Verdes Montenegro, L., et al. 2014, A&A, 567, A56
Serra, P., Koribalski, B., Duc, P.-A., et al. 2013, MNRAS, 428, 370
Serra, P., Westmeier, T., Giese, N., et al. 2015, MNRAS, 448, 1922
Sinha, M., & Holley-Bockelmann, K. 2012, ApJ, 751, 17
Smith, R., Sánchez-Janssen, R., Beasley, M. A., et al. 2015, MNRAS, 454, 2502
Sol Alonso, M., Lambas, D. G., Tissera, P., & Coldwell, G. 2006, MNRAS, 367, 1029
Stierwalt, S., Besla, G., Patton, D., et al. 2015, ApJ, 805, 2
Toomre, A., & Toomre, J. 1972, ApJ, 178, 623
Tortora, C., Napolitano, N. R., Cardone, V. F., et al. 2010, MNRAS, 407, 144
Tully, R. B. 1972, MNRAS, 159, 35P
Tully, R. B. 2015, AJ, 149, 171
Tully, R. B., Courtois, H. M., & Sorce, J. G. 2016, AJ, 152, 50
Tully, R. B., & Fouque, P. 1985, ApJS, 58, 67
Valluri, M. 1993, ApJ, 408, 57
van den Bosch, F. C., Aquino, D., Yang, X., et al. 2008, MNRAS, 387, 79
van den Bosch, F. C., Yang, X., Mo, H. J., et al. 2007, MNRAS, 376, 841
Veilleux, S., Cecil, G., & Bland-Hawthorn, J. 2005, ARA&A, 43, 769
Verdes-Montenegro, L., Yun, M. S., Williams, B. A., et al. 2001, A&A, 377, 812
Vollmer, B., Braine, J., Combes, F., & Sofue, Y. 2005, A&A, 441, 473
Vollmer, B., Cayatte, V., Balkowski, C., & Duschl, W. J. 2001, ApJ, 561, 708
Wang, E., Wang, J., Kauffmann, G., Józsa, G. I. G., & Li, C. 2015, MNRAS, 449, 2010
Wang, J., Catinella, B., Saintonge, A., et al. 2020, ApJ, 890, 63
Wang, J., Kauffmann, G., Overzier, R., et al. 2011, MNRAS, 412, 1081
Wang, J., Koribalski, B. S., Jarrett, T. H., et al. 2017, MNRAS, 472, 3029
Wang, J., Koribalski, B. S., Serra, P., et al. 2016, MNRAS, 460, 2143
Wang, J., Staveley-Smith, L., Westmeier, T., et al. 2021, ApJ, 915, 70
Wang, J., Xu, W., Lee, B., et al. 2020, ApJ, 903, 103
Watts, A. B., Catinella, B., Cortese, L., & Power, C. 2020a, MNRAS, 492, 3672
Watts, A. B., Power, C., Catinella, B., Cortese, L., & Stevens, A. R. H. 2020b, MNRAS, 499, 5205
Weinmann, S. M., van den Bosch, F. C., Yang, X., et al. 2006, MNRAS, 372, 1161
Westmeier, T., Kitaeff, S., Pallot, D., et al. 2021, MNRAS, 506, 3962
Wetzel, A. R., Tinker, J. L., Conroy, C., & van den Bosch, F. C. 2013, MNRAS, 432, 336
Whiting, M. 2020, in ASP Conf. Ser. 522, Astronomical Data Analysis Software and Systems XXVII (San Francisco, CA: ASP), 469
Willmer, C. N. A., Focardi, P., da Costa, L. N., & Pellegrini, P. S. 1989, AJ, 98, 1531
Wong, O. I., Stevens, A. R. H., For, B. Q., et al. 2021, MNRAS, 507, 2905
Wright, E. L., Eisenhardt, P. R. M., Mainzer, A., et al. 2010, AJ, 140, 1868
Wyder, T. K., Martin, D. C., Schiminovich, D., et al. 2007, ApJS, 173, 293
Yang, X., Mo, H. J., & van den Bosch, F. C. 2008, ApJ, 676, 248
York, D. G., Adelman, J., Anderson, J. E., Jr., et al. 2000, AJ, 120, 1579
Zasov, A. V., & Sulentic, J. W. 1994, ApJ, 430, 179
Zehavi, I., Zheng, Z., Weinberg, D. H., et al. 2005, ApJ, 630, 1
Zhang, H.-X., Hunter, D. A., Elmegreen, B. G., Gao, Y., & Schruba, A. 2012, AJ, 143, 47
Zhang, W., Li, C., Kauffmann, G., et al. 2009, MNRAS, 397, 1243
Zheng, Z., Wang, H., Ge, J., et al. 2017, MNRAS, 465, 4572
Zibetti, S., Charlot, S., & Rix, H.-W. 2009, MNRAS, 400, 1181
Zolotov, A., Dekel, A., Mandelker, N., et al. 2015, MNRAS, 450, 2327
Zuo, P., Xu, C. K., Yun, M. S., et al. 2018, ApJS, 237, 2